



HAL
open science

**Thermal history of Northwest Africa 5073–A
coarse-grained Stannern-trend eucrite containing
cm-sized pyroxenes and large zircon grains**

Julia Roszjar, Knut Metzler, Addi Bischoff, Jean-Alix J-A Barrat, Thorsten Geisler, R.C. Greenwood, I. A. Franchi, Stephan Klemme

► **To cite this version:**

Julia Roszjar, Knut Metzler, Addi Bischoff, Jean-Alix J-A Barrat, Thorsten Geisler, et al.. Thermal history of Northwest Africa 5073–A coarse-grained Stannern-trend eucrite containing cm-sized pyroxenes and large zircon grains. *Meteoritics and Planetary Science*, 2011, 46 (11), pp.1754-1773. 10.1111/j.1945-5100.2011.01265.x . insu-00637903

HAL Id: insu-00637903

<https://insu.hal.science/insu-00637903>

Submitted on 3 Apr 2012

HAL is a multi-disciplinary open access archive for the deposit and dissemination of scientific research documents, whether they are published or not. The documents may come from teaching and research institutions in France or abroad, or from public or private research centers.

L'archive ouverte pluridisciplinaire **HAL**, est destinée au dépôt et à la diffusion de documents scientifiques de niveau recherche, publiés ou non, émanant des établissements d'enseignement et de recherche français ou étrangers, des laboratoires publics ou privés.

1 **Thermal history of Northwest Africa (NWA) 5073**
2 **- a coarse-grained Stannern-trend eucrite containing cm-sized pyroxenes**
3 **and large zircon grains**
4
5
6
7

8 **Julia Roszjar¹, Knut Metzler¹, Addi Bischoff¹, Jean-Alix Barrat², Thorsten Geisler³,**
9 **Richard C. Greenwood⁴, Ian A. Franchi⁴, and Stephan Klemme⁵**

10
11 ¹Institut für Planetologie, Westfälische Wilhelms-Universität Münster, Wilhelm-Klemm-Str. 10, D-
12 48149 Münster, Germany (e-mail: j_rosz01@uni-muenster.de).
13

14 ²Université Européenne de Bretagne, Institut Universitaire Européen de la Mer, Place Nicolas
15 Copernic, 29280 Plouzané Dedex, France.
16

17 ³Steinmann Institut, Rheinische Friedrich-Wilhelms-Universität Bonn, Poppelsdorfer Schloß, 53115
18 Bonn, Germany
19

20 ⁴Planetary and Space Sciences Research Institute, The Open University, Milton Keynes, MK7 6AA,
21 UK.
22

23 ⁵Institut für Mineralogie, Westfälische Wilhelms-Universität Münster, Corrensstr. 24, D-48149
24 Münster, Germany.
25
26
27
28
29
30
31
32
33
34
35
36
37
38
39
40
41
42
43
44
45
46
47
48
49
50
51

52 **Abstract**

53 We report on the bulk chemical composition, petrology, oxygen isotopic composition, trace
54 element composition of silicates, and degree of self-irradiation damage on zircon grains of the eucrite
55 Northwest Africa (NWA) 5073, to constrain its formation and post-crystallization thermal history, and
56 to discuss their implications for the geologic history of its parent body. This unequilibrated and
57 unbrecciated meteorite is a new member of the rare Stannern-trend eucrites. It is mainly composed of
58 elongated, zoned pyroxene phenocrysts up to 1.2 cm, plagioclase laths up to 0.3 cm in length, and is
59 rich in mesostasis. The latter contains zircon grains up to 30 μm in diameter, metal, sulfide, tridymite,
60 and Ca-phosphates. Textural observations and silicate compositions coupled with the occurrence of
61 extraordinary Fe-rich olivine veins that are restricted to large pyroxene laths indicate that NWA 5073
62 underwent a complex thermal history. This is also supported by the annealed state of zircon grains
63 inferred from μ -Raman spectroscopic measurements along with U and Th data obtained by electron
64 probe microanalyses.

65
66
67
68
69
70
71
72
73
74
75
76
77
78
79
80
81
82
83
84
85
86
87
88
89
90
91
92
93
94
95
96
97
98

Keywords: eucrite, bulk chemistry, petrology, trace elements, oxygen isotopes, μ -Raman spectroscopy, zircon annealing

99 **Introduction**

100 The so-called HED suite of achondrites (Howardites, Eucrites, and Diogenites) makes up the
101 largest suite of igneous rocks available from any Solar System body besides the Earth and the Moon
102 (Mittlefehldt et al., 1998). Eucrites represent basaltic rocks and gabbroic cumulates, whereas
103 diogenites are ultramafic rocks (orthopyroxenites, olivine-bearing orthopyroxenites, harzburgites, and
104 dunites), mainly composed of orthopyroxene and olivine (e.g., Mittlefehldt et al., 1998; Beck and
105 McSween, 2010). Howardites are polymict breccias, consisting of various amounts of eucritic and
106 diogenitic lithologies. The close relationship between HEDs is convincingly supported by
107 petrographic, mineralogical, chemical, and isotopic evidences (see McSween et al., 2010 for a review),
108 and suggest that they derived from the same parent body, possibly the asteroid 4 Vesta (e.g., McCord
109 et al., 1970; Consolmagno and Drake, 1977; Binzel and Xu, 1993; Drake, 2001). However, a few
110 eucrites display unusual petrographic features and distinct oxygen isotopic compositions and could,
111 therefore, have originated from distinct parent bodies (e.g., Yamaguchi et al., 2002; Scott et al., 2009;
112 Gounelle et al., 2009; Bland et al., 2009). Eucrites are widely thought to represent either surface or
113 near-surface basaltic liquids (lava flows or shallow intrusions) or crystal accumulations from basaltic
114 liquids. Most eucrites experienced a complex post-crystallization history, including prolonged thermal
115 metamorphism that produced recrystallization textures and caused exsolution and inversion of
116 pyroxenes (e.g., Takeda and Graham, 1991; Metzler et al., 1995, Yamaguchi et al., 1996, 2009; Mayne
117 et al., 2009), and multiple impact events. Thus, many eucrites are brecciated, and were formed in the
118 regolith and mega-regolith of their parent body (e.g., Stöffler et al., 1988). They consist of mineral
119 and/or lithic fragments embedded in a fine-grained, generally fragmented matrix (e.g., Takeda and
120 Graham, 1991; Metzler et al., 1995; Bischoff et al., 2006; Llorca et al., 2009). From a chemical point
121 of view, eucrites can be subdivided into basaltic (noncumulate), and cumulate eucrites, both of which
122 occur also as clasts in polymict eucrites and howardites (e.g., Takeda, 1991). Cumulate eucrites are
123 coarse-grained rocks with high Mg-numbers [$Mg\# = \text{molar Mg}/(\text{Mg} + \text{Fe})$], low incompatible trace
124 element abundances compared to other eucrites, and pronounced positive Eu anomalies - a feature
125 consistent with plagioclase accumulation. Basaltic eucrites can be subdivided into three compositional
126 distinct groups on the basis of their $Mg\#$ or $\text{FeO}_{\text{total}}/\text{MgO}$ wt.% ratio, TiO_2 contents, and incompatible
127 trace element abundances (e.g., Stolper, 1977; Warren and Jerde, 1987; Mittlefehldt et al., 1998;
128 Yamaguchi et al., 2009): Main Group Nuevo Laredo-trend eucrites, Stannern-trend eucrites and the
129 residual eucrites. Main Group Nuevo Laredo-trend eucrites are the most common ones. They display
130 wide variations in $Mg\#$ with only moderate variations in incompatible element abundances. They are
131 believed to represent a fractional crystallization trend (e.g., Stolper, 1977; Warren and Jerde, 1987).
132 Stannern-trend eucrites are rare. They include three falls (Stannern, Bouvante, and Pomozdino), and
133 about a dozen finds from Antarctica (e.g., Y-75011) and from the Sahara (e.g., NWA 4523 and NWA
134 1000). They display the same major element abundances as the less evolved rocks of the Nuevo
135 Laredo group, but exhibit high Ti and incompatible trace element abundances, and significant negative

136 Eu, Sr, and Be anomalies. The origin of these eucrites is controversial. It has been proposed that the
137 Stannern-trend eucrites could have been generated from the same mantle source as Main Group
138 eucrites but at smaller degrees of partial melting, and possibly at slightly different oxygen fugacities
139 (Stolper, 1977; Mittlefehldt and Lindstrom, 2003). Alternatively, it has been proposed that the high
140 incompatible trace element abundances could be explained by an intricate in-situ crystallization
141 process (Barrat et al., 2000), or by the involvement of highly evolved KREEP-like melts (Warren and
142 Kallemeyn, 2001). The contamination of Main Group eucritic magmas might be also explained by
143 melts derived from partial melting of the asteroid's crust, which would can successfully explain both
144 the high incompatible trace elements concentrations and the distinctive Eu, Sr, and Be anomalies
145 shown by the Stannern-trend eucrites (Barrat et al., 2007). Finally, the residual eucrites display major
146 element abundances consistent with Main Group eucrites, but light REE depletions and positive Eu
147 anomalies. Partial melting followed by extraction of a few percent of partial melts can satisfactorily
148 explain these features (Yamaguchi et al., 2009). At present, it is generally thought that the
149 differentiation history of the eucrite parent body has been triggered by the formation of a global
150 magma ocean (e.g., Takeda, 1979; Righter and Drake, 1997; Ruzicka et al., 1997; Warren, 1997;
151 Greenwood et al., 2005). This hypothesis is at first glance consistent with the petrology of the eucrites,
152 but cannot easily account for the geochemistry of the diogenites (e.g., Mittlefehldt 2000; Barrat et al.,
153 2008, 2010). Thus, the magmatic and thermal histories of the parent body were certainly much more
154 complicated than generally believed and more detailed studies of HED meteorites are necessary to
155 further our understanding of the process leading to the formation of HED meteorite genesis. Recently,
156 we have identified NWA 5073, a eucrite which displays some unique features. This single,
157 unbrecciated stone is characterized by an unusual texture with cm-sized unequibrated pyroxenes
158 crosscut by numerous secondary olivine-rich veins, and mesostasis areas containing large zircon
159 grains. Here, we report on the bulk chemistry, petrology, and isotopic characteristics of this
160 exceptional meteorite and discuss its genesis and complex post-crystallization history. Preliminary
161 data on NWA 5073 have been previously presented by Roszjar et al. (2009a-c) and Roszjar and
162 Scherer (2010).

163

164 **Analytical Methods**

165 The textural and mineralogical investigations of the sample were performed by optical and
166 electron microscopy on a thin section (PL07217). Modal abundance of major phases and mesostasis
167 were determined based on multiple point-counting applied on a backscattered electron (BSE)
168 photomicrograph using an Olympus Analysis software. A JEOL A840 scanning electron microscope
169 (SEM) equipped with energy dispersive spectrometers (EDS; INCA; Oxford Instrument) at the
170 Interdisciplinary Center for Electron Microscopy and Microanalysis (ICEM) at the Westfälische
171 Wilhelms-Universität Münster was used for detailed petrographic investigations. Qualitative analyses
172 have been carried out using an acceleration voltage of 20 kV, and a beam current of 15 nA. High

173 contrast, low brightness BSE imaging has been used for systematic identification and localization of
174 Zr-bearing phases. Quantitative analyses of mineral compositions were obtained using a JEOL JXA
175 8900 Superprobe electron probe micro analyzer (EPMA) operated at an acceleration voltage and beam
176 current of 15 kV and 15 nA, respectively. Natural and synthetic standards of well-known compositions
177 were used as standards. Matrix corrections were made according to the $\Phi\rho(z)$ procedure of Armstrong
178 (1991).

179 Prior to micro-Raman spectroscopy, investigations of zircon grains were performed on the
180 JEOL A840 SEM at conditions described above. BSE imaging allowed selection of 10 appropriate
181 grains with sufficient diameter ranging from 10-25 μm that were free of cracks and inclusions, and
182 were representative of the whole zircon population in NWA 5073 in terms of mineral shape and
183 mineral paragenesis with surrounding phases. The same spots on individual zircon grains investigated
184 by Raman spectroscopy were subsequently analyzed for major, minor, and trace element
185 concentrations by wavelength-dispersive analysis using a Cameca SX 100 EPMA at the Institut für
186 Mineralogie, Universität Hamburg. Major (Si, Zr, Hf) and minor (Al, Fe, P, Ca, Mn, Y) elements were
187 analyzed in a first sequence using a beam current of 20 nA, an acceleration voltage of 15 keV, total
188 counting times of 30 s, and a beam diameter of 1-2 μm . Th and U concentrations were subsequently
189 determined in a separate cycle with total counting times of 600 s (10×60 s) for the U- M_{β} and Th- M_{α}
190 line, and a beam current and acceleration voltage of 200 nA and 15 kV, respectively, to achieve a
191 better precision. A small overlap of the Th- M_{α} on the U- M_{β} line was corrected using the method
192 proposed by Åmli & Griffin (1975). For these conditions the detection limit of U and Th is about 20-
193 30 ppm.

194 Micro-Raman spectroscopic measurements were performed subsequently, but prior to
195 compositional analysis by EPMA to preclude any possible irreversible modifications of the radiation-
196 damaged structure as a result of the electron beam impact. Micro-Raman spectroscopic analyses were
197 carried out on a polished, cleaned thin section of NWA 5073 using a Jobin Yvon HR800 dispersive
198 Raman spectrometer at the Institut für Anorganische und Analytische Chemie at the Westfälische
199 Wilhelms-Universität Münster. The 632.817 nm line of a Nd-YAG laser was used as excitation source
200 with a beam power of ~ 10 mW at the exit of the laser. The scattered Raman light was collected with a
201 100 times objective (N.A. =0.9) with charge-coupled device detector (CCD) after being dispersed by a
202 grating of 1800 grooves mm^{-1} . The spectrometer slit width was set to 150 μm , yielding a spectral
203 resolution of 1.9 cm^{-1} near 1000 cm^{-1} as determined from Ne light bands. The lateral resolution was
204 about 1-2 μm . A possible spectrometer drift was monitored by measuring the 520.7 cm^{-1} band of
205 silicon and the spectral lines of the Ne-lamp immediately before and after the sample analyses.
206 Information about the structural state of individual zircon grains was obtained by examining the total
207 spectrum and by monitoring the intensity, full width at half maximum (FWHM), and the frequency of
208 the internal antisymmetric $\nu_3(\text{SiO}_4)$ stretching mode located near 1008 cm^{-1} in a non-metamict zircon.
209 This band was monitored because (i) it has been shown that it is most suitable for quantifying

210 radiation damage (Wopenka et al., 1996; Nasdala et al., 1996; Nasdala et al., 1998; Palenik et al.,
211 2003), since it is the strongest Raman band of zircon and thus easy to measure precisely (Dawson et
212 al., 1971; Nasdala et al., 1996; Zhang et al., 2000a), and (ii) it is not significantly red-shifted by
213 impurity-related structural disorder such as caused by variations in the Hf concentration (Hoskin and
214 Rodgers, 1996). The broad band profile in the frequency region between 900 and 1100 cm^{-1} results
215 from an overlap of the $\nu_3(\text{SiO}_4)$ with the adjacent, internal $\nu_1(\text{SiO}_4)$ stretching mode (A_{1g} symmetry;
216 Dawson et al., 1971) at about 975 cm^{-1} and, in radiation-damaged zircon, from the contribution of a
217 broad background feature at a lower frequency, which has been assigned to the amorphous component
218 in metamict zircon (Zhang et al., 2000a). Quantitative band parameters were obtained by
219 deconvoluting the overall band profile in the frequency region between 800 and 1100 cm^{-1} with three
220 Voigt functions and a linear background as shown by Geisler et al. (2001). The reproducibility of the
221 fitted frequency is better than 0.2 cm^{-1} and that of the linewidth is in the order of $\pm 0.5 \text{ cm}^{-1}$ at a
222 linewidth smaller than 20 cm^{-1} and $\pm 1.0 \text{ cm}^{-1}$ for larger linewidths. The effect of the finite slit width on
223 the measured linewidth, given as the full width at half maximum (FWHM), was then corrected by the
224 method of Tanabe and Hiraishi (1980).

225 From radioactive decay of the ^{238}U , ^{235}U , and ^{232}Th isotopes, the number of α -decay events for
226 different U and Th concentrations were calculated according to the following equation:

$$227 \quad D_\alpha = 8 N_1 [\exp(\lambda_1 t - 1)] + 7 N_2 [\exp(\lambda_2 t - 1)] + 6 N_3 [\exp(\lambda_3 t - 1)] \quad (1)$$

228 where N_1 , N_2 , and N_3 are the present concentrations of ^{238}U , ^{235}U , and ^{232}Th in the zircon grains,
229 respectively, λ_1 , λ_2 , and λ_3 are the decay constants for ^{238}U , ^{235}U , and ^{232}Th in years⁻¹, respectively, and
230 t is the age of the zircon. For our calculations we assumed an age of 4.55 Ga.

231 The bulk chemical composition of NWA 5073 has been determined at the Institut
232 Universitaire Européen de la Mer (IUEM), Plouzané, using ~100 mg of powdered sample material.
233 The powdered whole rock fraction, derived from initially ~12 g sample material and devoid of fusion
234 crust, was precleaned with ethanol and ultra pure MilliQ® water in an ultrasonic bath, before it was
235 carefully crushed into small pieces in an agate mortar. Subsequently, a representative fraction of 0.48
236 g was powdered. About 100 mg of the latter were used for bulk rock analyses. Major elements (Ti, Al,
237 Cr, Fe, Mn, Mg, Ca, Na, K, and P) were determined by ICP-AES (inductively coupled plasma-atomic
238 emission spectrometry) using the procedure described by Cotten et al. (1995). The accuracy of this
239 system is better than 5%, and the reproducibility better than 3%. Trace element concentrations were
240 measured by ICP-MS (inductively coupled plasma-mass spectrometry) using a Thermo Element 2
241 spectrometer following the procedure described by Barrat et al. (2007). Based on standard
242 measurements and sample duplicates, trace element concentration reproducibility is generally better
243 than 5%, except for W, which is generally better than 10%.

244 Trace element abundances of pyroxenes and plagioclases in NWA 5073 were determined by
245 laser ablation-inductively coupled plasma-mass spectrometry (LA-ICP-MS) at the Institut
246 Universitaire Européen de la Mer, Plouzané. The analyses were performed under a He atmosphere

247 using an ArF-Excimer (193 nm wavelength) laser ablation system (Geolas Pro102), connected to a
248 Finnigan Thermo Element 2 spectrometer. Concentrations were determined on individual spots using a
249 60 μm -diameter laser beam and a laser repetition rate of 10 Hz. Background and peak were measured
250 for 40 s and 210 s, respectively. For all data, NIST 612 and BCR-2G glass standards were both used
251 for external calibration of relative element sensitivities, using values given by Jochum et al. (2005).
252 Replicate analyses of the USGS basaltic-glass standard BIR-1G run at intervals during the analytical
253 session, yielded an external reproducibility generally better than 5% (1σ relative standard deviation).
254 Analytical and data reduction procedures followed those described by Barrat et al. (2009). Results
255 were normalized to CaO abundances measured by electron microprobe as an internal standard to
256 account for variable ablation yield.

257 Oxygen isotope analysis was carried out at the Open University using an infrared laser
258 fluorination system (Miller et al., 1999). A 2 mg aliquot of NWA 5073, taken from a larger batch of
259 homogenized powdered sample material (~ 100 mg), was loaded in the sample chamber, together with
260 various international and internal oxygen isotope standards. To maximize yields and decrease the risk
261 of cross contamination, the powdered sample and standards were fused in vacuum to form a glass bead
262 prior to fluorination. O_2 was liberated by heating the glass beads using an infrared CO_2 laser ($10.6 \mu\text{m}$)
263 in the presence of 210 torr of BrF_3 . After fluorination, the O_2 released was purified by passing it
264 through two cryogenic nitrogen traps and over a bed of heated KBr. O_2 was analyzed using a
265 Micromass Prism III dual inlet mass spectrometer. Published system precision (1σ) (Miller et al.,
266 1999), based on replicate analyses of international (NBS-28 quartz, UWG-2 garnet) and internal
267 standards, is approximately $\pm 0.04\text{‰}$ for $\delta^{17}\text{O}$, $\pm 0.08\text{‰}$ for $\delta^{18}\text{O}$, and $\pm 0.02\text{‰}$ for $\Delta^{17}\text{O}$. Oxygen
268 isotope analyses are reported in standard δ -notation where $\delta^{18}\text{O}$ has been calculated as:

$$269 \quad \delta^{18}\text{O} = ((\delta^{18}\text{O}/\delta^{16}\text{O})_{\text{sample}}/(\delta^{18}\text{O}/\delta^{16}\text{O})_{\text{ref}}) - 1) \times 1000 \quad (2)$$

270 and similarly for $\delta^{17}\text{O}$ using $^{17}\text{O}/^{16}\text{O}$ ratio. $\Delta^{17}\text{O}$ has been calculated using the linearized format of
271 Miller (2002):

$$272 \quad \Delta^{17}\text{O} = 1000 \ln (1 + (\delta^{17}\text{O}/1000)) - \lambda 1000 \ln (1 + (\delta^{18}\text{O}/1000)) \quad (3)$$

273 with $\lambda = 0.5247$.

274

275 **Results**

276 *Mineralogy*

277 Northwest Africa 5073 is a desert find with a total mass of 185 g, representing an
278 unequilibrated, mesostasis-rich basaltic eucrite with the coarsest subophitic to slightly variolitic (fan-
279 spherulitic) texture among the known eucrites. It is an unbrecciated rock that preserved its
280 crystallization texture. It is mainly composed of elongated, unequilibrated pyroxene crystals up to 1.2
281 cm and plagioclase laths up to 0.3 cm in length (Fig. 1). Large phenocrysts of pyroxene make up
282 approximately 25 vol.% of the whole rock (Table 1). In variolitic areas, the plagioclase tends to be
283 skeletal, i.e., it occurs as partly hollow crystals, which is indicative of rapid cooling. Euhedral

284 chromite grains, occasionally dendritic, frequently occur with grain sizes up to 0.8 mm. Their
285 chemical composition (Table 2) is in the range of those for the unequilibrated eucrite Pasamonte
286 (Mittlefehldt et al., 1998). Fine-grained areas (mesostasis) that make up about 8.5 vol.% of the rock,
287 occur interstitially to the large crystals (Figs. 1 and 3). Terrestrial weathering of the sample is
288 indicated by the breakdown of about half of the metals and the occurrence of calcite, and Ba-sulfates
289 in some cracks all over the thin section. According to the scheme proposed for chondrites by Wlotzka
290 (1993), NWA 5073 is moderately weathered (W2-3).

291 Large pyroxene crystals are chemically unequilibrated with cores of $\text{En}_{51-60}\text{Fs}_{34-5}\text{Wo}_{2-8}$ and rims of
292 $\text{En}_{20-34}\text{Fs}_{42-63}\text{Wo}_{8-34}$ (Figs. 2 and 3; Table 2). The pyroxene composition depicted in Fig. 2, reflects
293 magmatic zoning from Mg-rich cores to Fe-rich rims of large pigeonite laths adjacent to surrounding
294 plagioclase crystals, which is typical of more rapidly cooled basalts containing pyroxene that has not
295 exsolved on a μm scale, e.g., Y-75011 (Takeda et al., 1994). As emphasized by e.g., Takeda et al.
296 (1982), chemical zoning in pyroxene primarily depends on the bulk chemistry of the basaltic melt and
297 on crystal-growth conditions such as the degree of supercooling and nucleation. Re-equilibration of
298 chemical zoning in pyroxene crystals did not occur in our sample. Thus, NWA 5073 was not formed
299 in a slow cooling environment, as indicated by the skeletal nature of plagioclases, (see Fig. 3a), and
300 was not affected by a long-term, high-temperature event, which would have resulted in re-
301 equilibration of pyroxene crystals. The large pyroxene crystals are frequently twinned and fractured
302 mainly perpendicular to the c-axis. This is in strong contrast to the adjacent plagioclase crystals which
303 do not show this fracturing. The small pyroxenes interstitial to the large crystals show similar Ca
304 contents as the rims of large crystals, but contain somewhat more Fe (Fig. 2, open squares, Table 2).

305 Occasionally, very thin ($<1\mu\text{m}$) exsolution lamellae of augite in the host pyroxenes can be observed
306 (e.g., Fig. 3). Pyroxenes in contact with the mesostasis frequently have a corroded appearance. Large
307 pyroxene grains are crosscut by fractures that are mainly filled by Fe-rich olivine. Originating from
308 these veins, a distinct Fe-enrichment of the adjacent host pigeonite can be observed, which clearly
309 parallels the veins (Fig. 3). Pyroxene areas distant to these veins appear as Mg-rich “cores”,
310 surrounded by Fe-enriched areas. These “cores” seem to have preserved their original composition
311 from primary crystallization ($\text{Fs}_{\sim 34}$). Additionally, Fe has effectively diffused from the olivine veins
312 and larger fractures devoid of olivine veins into the host pyroxene crystals along certain
313 crystallographic orientations, which probably represent cleavage plans (see Figs. 3d and 4a-b). Veins
314 of Fe-rich olivine (Fa_{65-71}) are clearly restricted to the large pyroxene crystals and always end abruptly
315 at their boundaries. These veins are very irregular with distinct thickness variations (Fig. 3a-c). The
316 olivine appears to have grown along preexisting fractures of its host pyroxene, while adjacent large
317 plagioclase crystals are devoid of it (Fig. 3a-c). Euhedral chromite, and troilite crystals, and sporadic
318 subrounded apatite grains occur within these veins (Fig. 3d). Similar olivine veins have been described
319 from a few other eucrites and howardites, namely Macibini, Y-7308, Y-790260, Y-75011, Y-82202,

320 NWA 049, NWA 1000, and NWA 2061 (Takeda and Yanai, 1982; Takeda et al., 1983; Metzler, 1985;
321 Warren, 2002; Barrat et al., 2011).

322 Two primary feldspar generations occur, namely large plagioclase laths (up to 3 mm in length) and
323 small plagioclase grains located in the mesostasis, both of which are compositionally in the typical
324 eucrite range (e.g., Mittlefehldt et al., 1998) of $An_{76-92}Ab_{8-22}Or_{0-3}$ (Fig. 5; Table 2). The plagioclases
325 found in mesostasis areas tend to be more Ab-rich compared to large plagioclase laths (Fig. 5). Many
326 large plagioclase crystals are clouded by myriads of exsolved tiny pyroxene and SiO_2 grains, as
327 commonly observed in eucrites (e.g., Harlow and Klimentidis, 1980; Metzler et al., 1995). Additional
328 to the primary plagioclases, we identified another, probably second generation of feldspars that are
329 typically An_{97-100} in composition (Fig. 5) and were usually found in association with Fe-rich olivine
330 veins within large pyroxene laths (Fig. 4).

331 The mesostasis consists of tridymite laths up to 0.8 mm, Ni-poor metallic Fe ($<300 \mu m$), ilmenite (<60
332 μm), chromite, plagioclase, augite, apatite, merrillite, troilite, zircon, baddeleyite, and very small
333 amounts of Fe-rich olivine. In addition, sporadic anorthite (An_{95}) was found. In some cases the
334 mesostasis areas are not well-defined and appear blurred. More than 30 grains of Zr-bearing phases,
335 such as zircon, baddeleyite, and zirconolite grains, with diameters ranging from 1 to 30 μm were
336 found in the mesostasis (Fig. 6; Roszjar et al., 2009b). They are typically located interstitial to
337 ilmenite, pyroxene, plagioclase, and iron metal, and/or occur as inclusions in ilmenite and are
338 subhedral to anhedral, and rounded in shape. The major element composition is consistent for all
339 analyzed zircon grains (see Table 2), and within the range of prior published data on eucrite zircon
340 grains (Saiki et al., 1990; Bukovanská et al., 1991; Ireland and Bukovanská, 1992; Yamaguchi et al.,
341 2001; Yamaguchi and Misawa 2001; Misawa et al., 2005; Barrat et al., 2007; Roszjar et al., 2009c). In
342 addition to BSE images that were taken for all selected zircon grains, cathodoluminescence images
343 were exemplarily taken for some of them. Here it was found that the luminescence behavior is distinct
344 from grain to grain. Nevertheless, some zircon grains are characterized by partial luminescence with a
345 preferred direction, increasing towards the edges of the grains, also giving evidence for a thermal
346 reaction front caused by a metamorphic event (Fig. 6).

347 *Shock features*

348 Northwest Africa 5073 as a whole is very weakly shocked, possibly equivalent to a S2 stage as
349 defined for chondrites (Stöffler et al., 1991; Bischoff and Stöffler, 1992). Evidence for shock is given
350 by the undulatory extinction of about half of the plagioclases and the occurrence of dislocation lines in
351 large pyroxene laths.

352 There is also evidence for an earlier shock event which affected this meteorite prior to annealing
353 during thermal metamorphism. Minor tiny, euhedral to subhedral troilite (FeS) grains and blebs of
354 metallic Fe-Ni that are usually $<3 \mu m$, occur within the plagioclase crystals and are arranged in
355 curvilinear trails, frequently aligned in a pearl chain manner, which do not follow the cleavage planes
356 and are restricted to the interiors of individual silicate crystals. It is known that metal and sulfide are

357 readily mobilized and re-precipitated in the shape of trails during shock metamorphism (Rubin, 1992).
358 These inclusions are in principle the cause of the silicate darkening which can be described as impact-
359 generated “shock darkening” (Rubin, 1992; Dodd, 1981). After annealing the metal and sulfide veins
360 are probably transformed to the tiny blebs described above.

361 *Bulk chemical composition*

362 The major and trace element abundances of NWA 5073 share similarities with other Stannern-
363 trend eucrites, such as Bouvante and Stannern (Table 3). Northwest Africa 5073 has respectively
364 $\text{FeO}_{\text{total}}/\text{MgO}$ ratio (2.31) and Sc concentration (25.8 $\mu\text{g/g}$) slightly lower, and MgO (8.70 wt%), Cr_2O_3
365 (0.59 wt%) concentrations higher to that of typical Main Group eucrites (e.g., Warren et al., 2009).
366 Similar “high” MgO abundances were previously measured on Pomozdino by Warren et al. (1990),
367 and led these authors to propose that this meteorite could be a partial cumulate. Moreover, an increase
368 of MgO can be produced by a slight oversampling of pyroxene in the powdered sample. Because
369 NWA 5073 is unequilibrated, these two possibilities can be easily discussed. We have calculated the
370 apparent distribution coefficient between the pigeonite cores (with $n = 27$) and the whole rock
371 composition ($K_D^{\text{Fe/Mg}} = (\text{Fe/Mg})_{\text{pigeonite core}}/(\text{Fe/Mg})_{\text{whole rock}}$). The result, $K_D^{\text{Fe/Mg}} = 0.32 \pm 0.01$ (2σ), is in
372 very good agreement with experimental distribution coefficients obtained for eucritic systems ($K_D^{\text{Fe/Mg}}$
373 $= 0.30$; Stolper, 1977). A lower value would have been obtained if the powder contained a pyroxene
374 excess. Thus, the pigeonite cores formed from a parental melt displaying the same Fe/Mg as the
375 analyzed powder. We conclude that the whole rock composition is probably close to its parental melt.
376 However, we suspect that the rather high Cr_2O_3 abundance is an artifact produced by a very small
377 excess of chromite in the powder.

378 Weathered meteorite finds from the Sahara generally exhibit marked Ba and Sr enrichments that are
379 sensitive indicators for the development of secondary phases (e.g., Stelzner et al., 1999; Barrat et al.,
380 2003; Crozaz et al., 2003). NWA 5073 is no exception, and displays high Ba and Sr concentrations
381 (177 $\mu\text{g/g}$ and 2131 $\mu\text{g/g}$, respectively). It should be noted that its Th/U ratio ($= 3.38$) and Pb
382 abundances ($= 0.24 \mu\text{g/g}$), which are other possible indicators of weathering, do not show perturbed
383 values.

384 Although NWA 5073 is characterized by a low FeO/MgO ratio (Fig. 7, Table 3), it displays high
385 levels of concentrations for incompatible elements, as exemplified by the REEs (Fig. 8). This suggests
386 that NWA 5073 is a new member of the Stannern-trend eucrites, transitional between the Main Group
387 and the REE-rich eucrites such as Stannern or Bouvante. Indeed, NWA 5073 exhibits a much more
388 pronounced negative Eu anomaly ($\text{Eu}/\text{Eu}^* = 0.68$) and a higher Gd/Lu ratio than a regular Main Group
389 or Nuevo Laredo eucrite, and its REE-pattern is parallel to those of the Stannern-trend eucrites (e.g.,
390 Bouvante and Stannern). These similarities extend to other incompatible trace element abundances,
391 and, interestingly, NWA 5073 displays a marked negative Be anomaly (Fig. 9) which is a distinctive
392 feature of the Stannern-trend eucrites (Barrat et al., 2007). Thus, we can deduce that NWA 5073 is
393 clearly a new member of this rare group of eucrites.

394 *Mineral chemical composition*

395 In addition to bulk rock trace elements, REE concentrations of pyroxenes and plagioclases
396 have been determined with LA-ICP-MS. Results are shown in Table 4. CI normalized REE patterns
397 for pyroxenes and plagioclases are presented in Fig. 10. In eucrites, pyroxene is one of the dominant
398 phases next to plagioclase, and a sensitive indicator of intrinsic variables such as oxygen fugacity and
399 temperature that may affect their crystallization sequence. Therefore, major, minor, and trace elements
400 have been investigated in order to decipher the evolution of the NWA 5073 meteorite. Rare earth
401 element abundances of selected pyroxene cores in NWA 5073 are in the range of $0.02\times$ (La) to $2.2\times$
402 (Lu) CI chondritic abundances, relative to the values given in Evensen et al. (1978), which is within
403 the range presented by Pun and Papike (1996). All analyzed pigeonite cores in NWA 5073 exhibit
404 variable REE abundances that correlate with Ca concentrations, and are generally HREE-enriched
405 with a pronounced negative Eu anomaly ($\text{Eu}/\text{Eu}^*=0.68$). A total of 7 plagioclase grains have been
406 analyzed for their REE abundances. The latter exhibit a pronounced positive Eu anomaly with Eu/Eu^*
407 = 61, thus are in agreement with the data range for eucrites previously reported in literature (e.g., Hsu
408 and Crozaz, 1996; Floss et al., 2000). The REE patterns of single plagioclases are slightly fractionated
409 with LREE being enriched. The total abundance of REE ranges from $2\times$ (La) to 0.1 (Er) \times CI
410 (Evensen et al., 1978), except for Eu (Table 4).

411 *Oxygen isotope composition*

412 The oxygen isotope composition of NWA 5073 obtained in this study ($\delta^{17}\text{O} = 1.89\text{‰}$, $\delta^{18}\text{O} =$
413 4.05‰ , $\Delta^{17}\text{O} = -0.24\text{‰}$) is plotted in Fig. 11 along with the data for other HED samples obtained by
414 Greenwood et al. (2005). The $\Delta^{17}\text{O}$ value for NWA 5073 is close to the average HED value of -0.239
415 ± 0.007 (1σ) obtained by Greenwood et al. (2005) and indicates that the meteorite is a normal member
416 of the HED suite (Roszjar et al., 2009a). NWA 5073 was not acid leached prior to oxygen isotope
417 analysis and has a slightly elevated $\delta^{18}\text{O}$ value compared to the eucrites analyzed by Greenwood et al.
418 (2005), which may reflect a small degree of terrestrial weathering. However, the $\delta^{18}\text{O}$ composition of
419 NWA 5073 is within the range obtained by Wiechert et al. (2004), which extends to $\delta^{18}\text{O}$ values of
420 4.5‰ .

421 *Structural state of zircon grains as obtained by Raman spectroscopy*

422 It has been demonstrated that micro-Raman spectroscopy is a powerful tool to quantify the
423 degree of self-irradiation damage in single zircon grains caused by the radioactive decay of
424 incorporated U and Th (metamictization) as well as the structural recovery by thermal annealing
425 (Nasdala et al., 1995, 1998, 2001; Wopenka et al., 1996; Zhang et al., 2000a- c; Geisler et al., 2001;
426 Geisler, 2002; Palenik et al., 2003). As already mentioned, the $\nu_3(\text{SiO}_4)$ band, reflecting antisymmetric
427 Si-O stretching motions of the SiO_4 tetrahedra, is particularly sensitive to structural changes associated
428 with self-irradiation. Raman measurements of zircon grains in sample NWA 5073 reveal a decreased
429 frequency and an increased broadening of the $\nu_3(\text{SiO}_4)$ band with increasing radiation dose (D ; Fig.
430 12) as calculated from the U and Th concentration measured by EPMA and an inferred age of 4.55 Ga

431 (Table 5). The frequency shift is attributed to an increase in interatomic distances, i.e., to a slight
432 expansion of the lattice of the crystalline domains, whereas the increase in linewidths is attributed to
433 the fact that the distribution of bond lengths and bond angles within and between SiO₄ tetrahedra
434 becomes increasingly irregular (Wopenka et al., 1996).

435 In the diagram linewidth (given as FWHM) vs. frequency of the $\nu_3(\text{SiO}_4)$ band all measurements plot
436 along the radiation damage trend (*RDT*; Fig. 13a) that is mainly defined by measurements from
437 variably self-irradiation-damaged, alluvial zircons from Sri Lanka (Geisler et al., 2001). Dry annealing
438 experiments with self-irradiation-damaged zircon revealed that episodically annealed samples plot
439 above the RDT (arrows in Fig. 13a). A comparison of Raman data from natural zircons with
440 experimental annealing trends thus allows recognizing episodically annealed zircons, provided that
441 post-annealing radiation damage did not completely obscure the annealing effect, i.e., did not push the
442 data points back to the RDT in the frequency versus linewidth diagram shown in Fig. 13a. This means
443 that most likely only relatively recent episodic annealing events are recognizable in this diagram.
444 However, the observed congruency with the RDT does not imply that the NWA 5073 zircons were not
445 annealed during their history. In fact, from the diagram linewidth of the $\nu_3(\text{SiO}_4)$ band vs. α -decay
446 dose (*D*; Fig.13b) it can be observed that all analyzed zircon grains from the NWA 5073 eucrite plot
447 consistently below the so-called damage accumulation curve, defined by Palenik et al. (2003).
448 Samples that have been neither episodically nor continuously annealed during their geological history
449 (i.e., that have accumulated the entire damage over their geologic history) should plot, within errors,
450 onto this accumulation trend. The observation that most of the measurements from zircon grains of
451 sample NWA 5073 plot significantly below this curve is unambiguous evidence that they were
452 thermally annealed (Palenik et al., 2003), either continuously for a prolonged period of time or
453 episodically as a result of a short time heating event. In the latter case, however, the heating event
454 must have occurred very early in their history.

455

456 **Discussion**

457 Most HED meteorites show textural and chemical evidence for extensive thermal annealing
458 after crystallization such as: Fe-Mg equilibration in pyroxenes, exsolution of Ca-pyroxenes within host
459 pigeonites, plagioclase and pyroxene clouding, and recrystallization of lithic clasts and clastic matrices
460 (e.g., Duke and Silver, 1967; Mason et al., 1979; Takeda and Graham, 1991; Metzler et al., 1995;
461 Yamaguchi et al., 1996; Bogard and Garrison, 2003; Llorca et al., 2009). Moreover, many eucrites
462 were brecciated and reheated by impacts (e.g., Metzler et al., 1995; Bogard and Garrison, 2003). In the
463 case of NWA 5073, the thermal history seems to be very complex. In the following, we discuss
464 possible scenarios to explain both chemical and textural characteristics of this sample.

465

466 **Formation of primary phases in a magma chamber and excavation**

467 Since NWA 5073 is a coarse-grained basaltic sample containing large, elongated pyroxene
468 crystals that preserved their igneous Mg-Fe zoning, we can infer that this sample derived from a
469 relatively fast cooling magma source. However, due to the texture and the composition of the crystals
470 (e.g., Al content), the cooling rate must have been slower than 1 °C/hour (Walker et al., 1978; Powell
471 et al., 1980). Large pyroxene laths might represent an early crystallized phase from a magma that
472 experienced fast excavation during volcanic eruption. The process of fast excavation is affiliated to
473 thermal and pressure relief that caused mechanical stress in preexisting pyroxene crystals, probably
474 leading to fracturing and bending of the crystals. A fast excavation of the magma onto the surface of
475 the parent body results in quenching of the melt. Thus, this explains the observed skeletal, and
476 seemingly cotectic crystallisation of silicates (pyroxenes and plagioclases) and other minor phases,
477 while leaving the large previously crystallized pyroxene crystals relatively unaffected.

478

479 **Episode of secondary annealing and rapid cooling**

480 Several mineralogical and chemical observations clearly indicate an episode of thermal
481 annealing that caused disturbance of the NWA 5073 sample: (1) disturbance of the Lu-Hf system, as
482 demonstrated by Roszjar and Scherer (2010), (2) Fe-diffusion along cracks and cleavage planes within
483 the zoned pyroxene crystals (Fig. 3b-d), and (3) recovery of the crystal structure of zircon grains (Fig.
484 13b). Based on these observations, it is possible to constrain the time-temperature conditions of the
485 reheating event which is discussed in the following.

486 The observation of Roszjar and Scherer (2010) that about half of the mineral fractions, mainly
487 pyroxene-rich fractions and the whole rock, form an isochron of 4.68 ± 0.14 (2σ) Ga, whereas the
488 other half, e.g., chromite, metal, plagioclase-rich fractions, define a secondary isochron of 4.31 ± 0.14
489 (2σ) Ga, is clear evidence that the Lu-Hf system in some minerals was disturbed. Since the time gap
490 between the primary crystallisation of the eucrite and the event that disturbed the Lu-Hf system is at
491 least ~ 370 Ma, thermal metamorphism, driven by internal heat on the parent body, can be ruled out as
492 the cause for the isotope resetting. On the contrary, it is rather likely that the thermal event was short
493 and intensive. This is supported by the observations that (i) the primary pyroxenes preserved their
494 initial magmatic Mg-Fe-Ca zoning, (ii) the exsolution lamellae of augite in the host pyroxene grains
495 are very thin ($<1\mu\text{m}$), (iii) and the mesostasis shows a fine-grained subophitic texture. A short, but
496 intense heating event more than 300 Ma after the primary crystallization of the eucrite is only
497 conceivable by a shock-triggered process, e.g., by a superheated impact melt produced by a large
498 impact. The impact melt could have been injected into neighbouring target rock lithologies, causing a
499 short thermal pulse followed by fast cooling. Fast cooling is indicated by the absence of
500 recrystallization textures, which have neither been observed in the coarse mineral grains nor in the
501 fine-grained mesostasis. As discussed by Yamaguchi and Mikouchi (2005) small fractions of melt can
502 be formed when a eucrite is heated to a temperature slightly above its solidus of about 1100°C
503 (Stolper, 1977) for a short period of time. However, a temperature above the solidus would have

504 caused re-melting of mesostasis components, and a depletion of light rare earth elements (LREE) of
505 the whole rock, which has not been observed (Fig. 8). This suggests that the NWA 5073 sample was in
506 fact reheated to a certain degree for a short period of time, but most likely not re-melted. The absence
507 of any evidence for partial re-melting constrains the maximum annealing temperature to about
508 1100°C.

509 Assuming a maximum reheating temperature of 1100°C and that the reheating process possibly also
510 triggered Fe-diffusion along cracks and cleavage planes in large pyroxenes (Fig. 3d), the duration of
511 the heating event can now be estimated from the relation $L_D = 2\sqrt{Dt}$, where L_D is the diffusion length,
512 D the diffusion coefficient for Fe-diffusion in pyroxene, and t the diffusion time. From BSE images
513 (e.g., Fig. 3d), we measured an average diffusion path length, L_D , of about 25 µm for Fe-diffusion
514 between the Fe-rich olivine veins into the pyroxene. Using published diffusion coefficients for Fe-Mg
515 diffusion in pyroxene (Freer, 1981; Cherniak and Dimanov, 2010; Ganguly and Tazzoli, 1994), we
516 estimated that the heating to a temperature of about ~1100°C could have only lasted for some hours (5
517 hours at most). This order of magnitude for the duration of the reheating event obtained from this
518 back-of-the-envelope calculation is also consistent with the observation that the pigeonite pyroxenes
519 still show chemical zoning, i.e., were not re-equilibrated. It is noted that the order of magnitude of
520 hours would also hold for slightly longer diffusion lengths and slightly lower temperatures.

521 Probably the most convincing evidence for a secondary heating event is given by the Raman
522 measurements of ten zircon grains. In the plot of the linewidth of the $\nu_3(\text{SiO}_4)$ stretching band near
523 1008 cm^{-1} , expressed as the full width at half maximum (FWHM), versus the calculated radiation dose
524 of a single zircon grain (D), most analyzed points plot below the radiation damage accumulation curve
525 (Fig. 13b). We recall that samples that have neither been episodically nor continuously annealed
526 during their geological history and accumulated the entire structural damage should plot on this curve.
527 Laboratory dry annealing experiments with radiation-damaged zircon revealed that the temperature
528 and duration of a thermal event determines the degree of structural recovery that occurs after a certain
529 degree of structural damage has been accumulated, i.e., during an episodic annealing event (Geisler et
530 al., 2001; Geisler, 2002). Considering the low U and Th concentrations measured today, the zircons
531 accumulated only a limited amount of radiation damage during the first 370 Ma after their
532 crystallisation in the eucrite melt. Experimental work has shown that significant structural recovery of
533 less self-irradiation-damaged samples within time scales of a few hours only occurs at temperature in
534 excess of about 900°C (Geisler et al., 2001; Zhang et al., 2000b; Geisler, 2002). It is thus likely that
535 the actual temperature of the event affecting the NWA 5073 eucrite was between 900 and 1100°C.

536

537 **Formation of olivine-rich veins**

538 The occurrence of veins composed of Fe-rich olivine, secondary plagioclase, and small troilite
539 and chromite grains inside these veins within large pyroxene phenocrysts (Fig. 3) requires careful
540 consideration, especially as recent papers have suggested that minerals in these veins might have

541 crystallized from fluids or gases during a metasomatic reaction (Barrat et al., 2011). At this point we
542 would like to make very clear that the authors have rather different views concerning the formation of
543 the olivine-rich veins within the cores of pyroxene. Thus, we try to unravel the origin of the olivine-
544 rich veins in NWA 5073, suggesting two valid possible mechanisms of formation that will be
545 discussed separately in the following paragraphs:

546

547 **(a) Formation of the olivine-rich veins in NWA 5073 by metasomatism**

548 Based on distinct mineralogical features in eucrites, Barrat et al. (2011) defined a three-type
549 classification scheme for secondary alteration. The first type is characterized by Fe-enrichment along
550 cracks that cross cut large pyroxene crystals, and by occasional occurrence of Fe-rich olivine in some
551 fractures (e.g., Pasamonte). The second type reveals involves deposits of Fe-rich olivine (Fa₆₄₋₈₆) and
552 minor amounts of troilite inside the cracks as well as the sporadic occurrence of secondary Ca-rich
553 plagioclase (An₉₇₋₉₈) associated with Fe-rich olivine (NWA 2061, Y-75011, and Y-82202). The third
554 type is identifiable by a more frequent occurrence of Ca-rich secondary plagioclase, partial fillings of
555 cracks or rims of primary plagioclases with small crystals of secondary plagioclase, and Fe-enrichment
556 of pyroxenes accompanied by significantly decreased Al contents (NWA 049; Barrat et al., 2011).
557 According to this scheme, NWA 5073 belongs to the second type, as it contains secondary plagioclase
558 (An₉₇₋₁₀₀) associated with Fe-rich olivine veins, typically located at the grain boundaries between
559 larger primary plagioclase and large pyroxene laths. Based on these observations, Barrat et al. (2011)
560 proposed that Fe-rich olivine veins may be secondary precipitation products formed by the interaction
561 between pyroxene crystals and Fe-rich gas or fluid phases that invaded the pyroxene crystals along
562 fractures and offset planes. The chemical composition of the metasomatic agent is at present not well
563 constrained but could have been aqueous (Barrat et al., 2011).

564

565 **(b) Formation of the olivine-rich veins in NWA 5073 by incongruent melting**

566 The large pyroxene crystals contain olivine-rich veins that abruptly end at their margins (Fig.
567 3a-c). The Fe-rich olivine within these veins is accompanied by An-rich plagioclase, and small Cr-rich
568 oxides (chromites) and troilites. As shown in Fig. 3, all other adjacent silicate phases (small pyroxenes
569 and large plagioclases) are devoid of these veins. We believe that the chromites may be of genetic
570 significance, as it is known that the solubility of Cr³⁺ in silicate melts is rather high and Cr³⁺ is
571 immobile in hydrous fluids (e.g., Roeder and Reynolds, 1991). Thus, mobilization and precipitation of
572 small chromite grains in the olivine-rich veins found in NWA 5073 seems to indicate a magmatic
573 albeit secondary origin. As an alternative to the arguments presented in the previous paragraph, it may
574 have been that veins of olivine, anorthite, and Cr-rich oxides were formed by incongruent *in-situ*
575 melting of pyroxene (Fs₃₄Wo₂) at a temperature slightly above the temperature of formation of
576 primary, Mg-rich pigeonites, i.e. at about 1150°C (Stolper, 1977). This is suggested to have taken
577 place during a short period of a small temperature excursion in the magma chamber. The process of

578 incongruent melting must have taken place after formation of primary pyroxenes in the magma
579 chamber, but prior to excavation of the sample. During this peritectic reaction, olivine forms and the
580 remaining melt crystallizes minor, extremely Ca-rich plagioclase. A similar process of incongruent
581 melting of pigeonites producing olivine (Fo₃₅₋₅₅) plus silica was experimentally shown by e.g.,
582 Huebner et al. (1973) and Huebner and Turnock (1980). It should be noted that the experimental data
583 confirm that the olivines in the veins (Fa₆₅₋₇₁) are in equilibrium with the outer rims of large pyroxene
584 grains and the small pyroxenes (~Fs₆₂₋₆₈; Table 2). Since the pyroxene, which melts incongruently,
585 does not contain significant Na, the crystallizing plagioclase has to be low in Na and, consequently,
586 extremely rich in Ca (An₉₇₋₁₀₀). Cr- and S-rich oxides that are found within the olivine-rich veins are
587 sometimes also located within the primary pyroxenes. The incongruent melting of pigeonite requires
588 only a few tens of degrees above the peritectic temperature, so that if we employ the aforementioned
589 experimental data we estimate some 1150°C for the formation of the olivine veins in this scenario.

590

591 In summary, it seems that both interpretations for the formation of olivine-rich veins in large
592 pyroxenes, as discussed above, have some inconsistencies which cannot be resolved at this point. The
593 metasomatism model cannot fully explain the occurrence of Fe-rich olivine veins in large pyroxene
594 phenocrysts, while the adjacent silicate phases (small pyroxenes and large plagioclases) are devoid of
595 them. Furthermore, the occurrence of chromite within these veins is hardly explained by metasomatic
596 fluids. On the other hand, the model which involves incongruent melting cannot readily explain certain
597 textural observations, such as the only minor occurrence of olivine-rich veins in contact with
598 plagioclase. To unravel the process which leads to the formation of such Fe-rich olivine veins in large
599 pyroxenes, one would need further oxygen isotope data of these veins. Furthermore, more realistic
600 melting experiments on bulk eucrite samples and pyroxenes would be helpful.

601

602 **Pairing or launch-pairing of some Stannern-trend eucrites?**

603 According to sample textures, grain sizes, including the occurrence of Fe-rich olivine veins in
604 large pyroxenes and secondary plagioclases, NWA 5073 resembles some other Stannern-trend eucrite
605 finds from the Sahara, namely NWA 1000 and NWA 2061. Since the occurrence of Fe-rich olivine
606 veins in large pyroxene crystals is not restricted to the NWA 5073 sample, but was also found to occur
607 in other eucrites and howardites, namely Y-7308, Y-790260, Y-75011, and NWA 1000, Macibini, and
608 NWA 2061 (Takeda and Yanai, 1982; Takeda et al., 1983; Metzler, 1985; Warren, 2002; Barrat et al.,
609 2007; and Barrat, unpublished data), one can argue that these findings give some evidence for a large-
610 scale but certainly not global parent body process. However, NWA 1000 is severely shocked (S4), as
611 documented by the transformation of half of the plagioclase into maskelynite (Warren, 2002). Thus,
612 NWA 5073 and NWA 1000 are certainly not fall-paired. Since NWA 2061 is as REE-rich as Stannern
613 and thus distinct to NWA 5073, a pairing between those eucrites and NWA 5073 seems unlikely.
614 However a certain pairing, especially for the Stannern-trend eucrite finds with the NWA 5073 sample,

615 can only be unequivocally proven by obtaining noble gas exposure ages. However, some of these
616 samples may be launch-paired.

617

618 **Summary and Conclusions**

619 In summary, our results are: (i) Northwest Africa 5073 is a coarse-grained basaltic,
620 unequilibrated, and non-brecciated eucrite with a subophitic to slightly variolitic (fan-spherulitic)
621 texture, mainly composed of small equilibrated pyroxenes (~40 vol.%), elongated, unequilibrated
622 pyroxene phenocrysts up to 1.2 cm (~ 25 vol.%), plagioclase laths up to 0.3 cm in apparent length
623 (~26 vol. %), and about 8.5 vol.% mesostasis. (ii) This sample is very weakly shocked and moderately
624 weathered (W2-3). (iii) Based on its oxygen isotope composition ($\delta^{17}\text{O} = 1.88 \text{ ‰}$, $\delta^{18}\text{O} = 4.05 \text{ ‰}$,
625 $\Delta^{17}\text{O} = -0.239 \text{ ‰}$), we can deduce that NWA 5073 is a normal member of the HED suite of
626 achondrites. (iv) The large unequilibrated pyroxenes preserved their initial magmatic Mg-Fe-Ca
627 zoning and are crosscut by olivine-rich veins (Fa_{65-71}) which are restricted to them. These veins also
628 contain minor chromite, troilite, and very Ca-rich plagioclase. (v) Three different plagioclase
629 generations occur: (a) large primary plagioclases crystals ($\text{An}_{76-92}\text{Ab}_{8-22}\text{Or}_{0-3}$), (b) small primary
630 plagioclase grains of similar composition as the large ones that are concentrated in mesostasis areas
631 and, (c) a secondary generation of small plagioclases (An_{97-100}), typically 5-20 μm in diameter, always
632 found in association with Fe-rich olivine veins. (vi) Due to the occurrence of these olivine-rich veins
633 in large pyroxene crystals and the sporadic occurrence of secondary plagioclase associated with the
634 former, NWA 5073 belongs to stage 2-type eucrites, according to the classification scheme for
635 secondary alteration as proposed by Barrat et al. (2011). Other members of this group include NWA
636 2061, Y-75001, Y-82202, and probably NWA 1000 (Barrat et al., 2011). (vii) Based on its bulk
637 chemical composition (e.g., high Ti with $\text{TiO}_2 = 0.77 \text{ wt.}\%$, $\text{La} = 4.18 \text{ }\mu\text{g/g}$, negative Be anomaly),
638 NWA 5073 displays a distinctive Stannern-trend signature. (viii) The REE pattern of NWA 5073 bulk
639 rock, which is characterized by flat LREE and a slight HREE-depletion ($\text{La}_n/\text{Yb}_n=1.38$) with a
640 pronounced negative Eu anomaly ($\text{Eu}/\text{Eu}^*=0.68$), resembles those of other Stannern-trend eucrites.
641 (ix) Northwest Africa 5073 contains zircon grains up to 30 μm in size that were invariably found in
642 the mesostasis. These zircon grains are metamict and were annealed, indicating a short high-
643 temperature event (probably induced by shock) occurring after primary crystallization of main sample
644 constituents. (x) A short but intense heating event that caused disturbance of the sample is also
645 indicated by the disturbance of the Lu-Hf system, and Fe-diffusion along cracks and cleavage planes
646 within unequilibrated pyroxene crystals. (xi) According to sample textures, grain sizes, and the degree
647 of alteration, including the occurrence of olivine-rich veins in large pyroxenes, as well as secondary
648 plagioclases, NWA 5073 resembles some other Stannern-trend eucrite finds from the Sahara, namely
649 NWA 1000, NWA 2061 and NWA 4523. However, these four samples are unlikely fall-paired as
650 discussed above.

651

652 **Acknowledgements**

653 The authors are grateful to A. Yamaguchi and an anonymous reviewer for their helpful reviews, which
654 helped improving the paper and A. Ruzicka for thoughtful comments and for handling this article. We
655 also thank U. Heitmann for sample preparation, C. Bollinger for assistance at the LA-ICP-MS, J.
656 Berndt for guidance with the electron microprobe, and M. Menneken for help with Raman
657 measurements. This study was partially supported by the German Research Foundation (DFG; grant
658 Bi 344/9-1) and T. Geisler acknowledges a Heisenberg scholarship from the DFG.

659

660 **References**

661 Åmli R. and Griffin W. L. 1975. Microprobe analysis of REE minerals using empirical correction
662 factors. *American Mineralogist* 60:599-606.

663

664 Armstrong J. T. 1991. Quantitative elemental analysis of individual microparticles with electron beam
665 instruments. *Electron Probe Quantitation*, edited by Heinrich K. F. J. and Newbury D. E. New
666 York: Plenum Press. pp. 261-315.

667

668 Barrat J. A., Blichert-Toft J., Gillet Ph. and Keller F. 2000. The differentiation of eucrites: the role of
669 in-situ crystallization. *Meteoritics & Planetary Science* 35:1087-1100.

670

671 Barrat J. A., Jambon A., Bohn M., Blichert-Toft J., Sautter V., Göpel C., Gillet Ph., Boudouma O. and
672 Keller F. 2003. Petrology and geochemistry of the unbrecciated achondrite North West Africa
673 1240 (NWA 1240): an HED parent body impact melt. *Geochimica et Cosmochimica Acta* 67:3959-
674 3970.

675

676 Barrat J. A., Yamaguchi A., Greenwood R. C., Bohn M., Cotten J., Benoit M., and Franchi I. A. 2007.
677 The Stannern trend eucrites: contamination of main group eucritic magmas by crustal partial melts.
678 *Geochimica et Cosmochimica Acta* 71:4108-4124.

679

680 Barrat J. A., Yamaguchi A., Benoit M., Cotten J. and Bohn M. 2008. Geochemistry of diogenites: Still
681 more 392 diversity in their parental melts. *Meteoritics & Planetary Science* 43:1759-1775.

682

683 Barrat J. A., Yamaguchi A., Greenwood R. C., Bollinger C., Bohn M., and Franchi I. A. 2009. Trace
684 element geochemistry of K-rich impact spherules from howardites. *Geochimica et Cosmochimica*
685 *Acta* 73:5944-5958.

686

687 Barrat J.A., Yamaguchi A., Zanda B., Bollinger C., Bohn M. (2010) Relative chronology of crust
688 formation on asteroid 4-Vesta: Insights from the geochemistry of diogenites. *Geochimica et*
689 *Cosmochimica Acta* 74:6218-6231.

690

691 Barrat J. A., Yamaguchi A., Bunch T. E., Bohn M., Bollinger C., and Ceuleneer G. 2011. Possible
692 fluid-rock interactions on differentiated asteroids recorded in eucrite eucritic meteorites.
693 *Geochimica et Cosmochimica Acta* 75:3839-3852.

694

695 Beck A. W. and McSween H. Y. Jr. 2010. Diogenites as polymict breccias composed of
696 orthopyroxenite and harzburgite. *Meteoritics & Planetary Science* 45:850-872.

697

698 Binzel R. P. and Xu S. 1993. Chips off of Asteroid 4 Vesta: Evidence for the parent body of basaltic
699 achondrite meteorites. *Science* 260:186-191.

700

701 Bischoff A. and Stöffler D. 1992. Shock metamorphism as a fundamental process in the evolution of
702 planetary bodies: Information from meteorites. *European Journal of Mineralogy* 4:707-755.

703
704 Bischoff A., Scott E. R. D., Metzler K., and Goodrich C. A. 2006. Nature and origins of meteoritic
705 breccias. *Meteorites and the early solar system II*, edited by Lauretta D.S. and McSween H.Y.
706 Tucson: The University of Arizona Press. pp 679-712.
707
708 Bland P. A., Spurný P., Towner M. C., Bevan A. W. R., Singleton A. T., Bottke W.F. Jr., Greenwood
709 R. C., Chesley S. R., Shrubny L., Borovička J., Ceplecha Z., McClafferty T. P., Vaughan D.,
710 Benedix G. K., Deacon G., Howard K. T., Franchi I. A., Hough R. M. 2009. An anomalous basaltic
711 meteorite from the innermost main belt. *Science* 325:1525-1527.
712
713 Bogard D. and Garrison D. 2003. ^{39}Ar - ^{40}Ar ages of eucrites and thermal history of asteroid 4 Vesta.
714 *Meteoritics & Planetary Science* 38:669-710.
715
716 Bukovanská M., Ireland T. R., El Goresy A., Palme H., Spettel B., and Wlotzka F. 1991. Zircons in
717 the Padvarnikai brecciated eucrite (abstract). *Meteoritics* 26:325.
718
719 Cherniak D. J. and Dimanov A. 2010. Diffusion in pyroxene, mica and amphibole. *Reviews in*
720 *Mineralogy & Geochemistry* 72:641-690.
721
722 Consolmagno G. J. and Drake M. J. 1977. Composition and evolution of the eucrite parent body:
723 Evidence from rare earth elements. *Geochimica et Cosmochimica Acta* 41:1271-1282.
724
725 Cotten J., Ledez A., Bau M., Caroff M., Maury R. C., Dulski P., Fourcade S., Bohn M., and Brousse
726 R. 1995. Origin of anomalous Rare-Earth Element and Yttrium enrichments in subaerially exposed
727 basalts - Evidence from French-Polynesia. *Chemical Geology* 119:115-138.
728
729 Crozaz G., Floss C. and Wadhwa M. 2003. Chemical alteration and REE mobilization in meteorites
730 from hot and cold deserts. *Geochimica et Cosmochimica Acta* 67:4727-4741.
731
732 Dawson P., Hargreave M. M., and Wilkinson G. R. 1971. The vibrational spectrum of zircon (ZrSiO_4).
733 *Journal of Physics C: Solid State Physics* 4:240-256.
734
735 Dodd R. T. 1981. Meteorites- A Petrologic-Chemical Synthesis. *Cambridge University Press, New*
736 *York, New York, USA, 368 p.*
737
738 Drake M.J. 2001. The eucrite/Vesta story. *Meteoritics & Planetary Science* 36:501-513.
739
740 Duke M. B., and Silver L. T. 1967. Petrology of eucrites, howardites and mesosiderites. *Geochimica et*
741 *Cosmochimica Acta* 31:1637-1665.
742
743 Evensen N. M., Hamilton P. J., and O'Nions R. K. 1978. Rare Earth abundances in chondritic
744 meteorites. *Geochimica et Cosmochimica Acta* 42:1199-1212.
745
746 Floss C., Crozaz G., Yamaguchi A., and Keil K. 2000. Trace element constraints on the origins of
747 highly metamorphosed Antarctic eucrites. *Antarctic Meteorite Research* 13:222-237.
748
749 Freer R. 1981. Diffusion in Silicate Minerals and Glasses: A Data Digest and Guide to the Literature.
750 *Contributions to Mineralogy and Petrology* 76:440-454.
751
752 Ganguly J. and Tazzoli V. 1994. Fe^{2+} -Mg interdiffusion in orthopyroxene: Retrieval from the data on
753 intracrystalline exchange reaction. *American Mineralogist* 79:930-937.
754
755 Geisler T. 2002. Isothermal annealing of partially metamict zircon: evidence for a three-stage recovery
756 process. *Physics and Chemistry of Minerals*. 29:420-429.
757

758 Geisler T., Pidgeon R. T., van Bronswijk W., and Pleysier R. 2001. Kinetics of thermal recovery and
759 recrystallization of partially metamict zircon: a Raman spectroscopic study. *European Journal of*
760 *Mineralogy* 13:1163-1176.
761

762 Gounelle M., Chaussidon M., Morbidelli A., Barrat J. A., Engrand C., Zolensky M. E. and McKeegan
763 K. D. 2009. A unique basaltic micrometeorite expands the inventory of solar system planetary
764 crusts. *Proceedings of the National Academy of Sciences of the United States of America* 106:6904-
765 6909.
766

767 Greenwood R. C., Franchi I. A., Jambon A., and Buchanan P. C. 2005. Widespread magma oceans on
768 asteroidal bodies in the early Solar System. *Nature* 435:916-918.
769

770 Harlow G. E. and Klimentidis R. 1980. Clouding of pyroxene and plagioclase in eucrites: implications
771 for post-crystallization processing. *Proceedings, 11th Lunar Science Conference*. pp. 1131-1148.
772

773 Hoskin P. W. O. and Rodgers K. A. 1996. Raman spectral shift in the isomorphous series (Zr_{1-x}Hf_x)SiO₄. *European Journal of Solid State Inorganic Chemistry* 33:1111-1121.
774
775

776 Huebner J. S. and Turnock A. C. 1980. The melting relations at 1bar of pyroxenes composed largely
777 of Ca-, Mg-, and Fe-bearing components. *American Mineralogist* 65:225-271.
778

779 Huebner J. S., Ross M., Hickling N. 1973. Partial melting of pyroxenes and the origin of mare basalts
780 (abstract), *Lunar and Planetary Conference* 4:397-399.
781

782 Hsu W. and Crozaz G. 1996. Mineral chemistry and the petrogenesis of eucrites: I. Noncumulate
783 eucrites. *Geochimica et Cosmochimica Acta* 60:4571-4591.
784

785 Ireland T. R. and Bukovanskà M. 1992. Zircons from the Stannern eucrite (abstract). *Meteoritics*
786 27:237.
787

788 Jochum K. P., Willbold M., Raczeck I., Stoll B., and Herwig K. 2005. Chemical characterisation of
789 the USGS reference glasses GSA-1G, GSC-1G, GSD-1G, GSE-1G, BCR2-G, BHVO2-G, and
790 BIR1-G using EPMA, ID-TIMS, ID-ICP-MS and LA-ICP-MS. *Geostandards and Geoanalytical*
791 *Research* 29:285-302.
792

793 Llorca J., Casanova I., Trigo-Rodriguez J. M., Madeido J. M., Roszjar J., Bischoff A., Ott U., Franchi
794 I. A., Greenwood R. C., and Laubenstein M. 2009. The Puerte Lápice eucrite. *Meteoritics &*
795 *Planetary Science* 44:159-174.
796

797 Mason B., Jarosewich E., and Nelen J. A. 1979. The pyroxene-plagioclase achondrites. *Smithsonian*
798 *Contributions to the Earth Sciences* 22:27-45.
799

800 Mayne R. G., McSween H. Y., Jr., McCoy T. J., Gale A. 2009. Petrology of the unbrecciated eucrites.
801 *Geochimica et Cosmochimica Acta* 73:794-819.
802

803 McCord T. B., Adams J. B., and Johnson T.V. 1970. Asteroid Vesta: Spectral reflectivity and
804 compositional implications. *Science* 168:1445-1447.
805

806 McSween H. Y. Jr., Mittlefehldt D. W., Beck A. B., Mayne R. G., McCoy T. J. 2010. HED Meteorites
807 and their relationship to the geology of Vesta and Dawn mission. *Space Science Reviews*. 34p.
808

809 Metzler, K. 1985. Gefüge und Zusammensetzung von Gesteinsfragmenten in polymikten
810 achondritischen Breccien. *Diploma thesis*, University of Münster, 150 pp.
811

812 Metzler K., Bobe K. D., Palme H., Spettel B., and Stöffler D. 1995. Thermal and impact
813 metamorphism on the HED parent asteroid. *Planetary and Space Science* 43:499-525.

814
815 Miller M. F. 2002. Isotopic fractionation and the quantification of ^{17}O anomalies in the oxygen three-
816 isotope system: an appraisal and geochemical significance. *Geochimica et Cosmochimica Acta*
817 66:1881-1889.
818
819 Miller M. F., Franchi I. A., Sexton A. S., and Pillinger C. T. 1999. High precision $\delta^{17}\text{O}$ isotope
820 measurements of oxygen from silicates and other oxides: Method and Applications. *Rapid*
821 *Communications in Mass Spectrometry* 13:1211-1217.
822
823 Misawa K., Yamaguchi A., and Kaiden H. 2005. U-Pb and ^{207}Pb - ^{206}Pb ages of zircons from basaltic
824 eucrites: Implications for early basaltic volcanism on the eucrite parent body. *Geochimica et*
825 *Cosmochimica Acta* 69:5847-5861.
826
827 Mittlefehldt D. W. 2000. Petrology and geochemistry of the Elephant Moraine A79002 diogenite: A
828 genomict breccia containing a magnesian harzburgite component. *Meteoritics & Planetary Science*
829 35:901-912.
830
831 Mittlefehldt D. W. and Lindstrom M. M. 2003. Geochemistry of eucrites: genesis of basaltic eucrites,
832 and Hf and Ta as petrogenetic indicators for altered Antarctic eucrites. *Geochimica et*
833 *Cosmochimica Acta* 67:1911-1935.
834
835 Mittlefehldt D. W., McCoy T. J., Goodrich C. A., and Kracher A. 1998. Non-chondritic meteorites
836 from asteroidal bodies. In *Reviews in Mineralogy*, edited by Papike J. J., vol 36. Washington D. C.:
837 Mineralogical Society of America. pp. 4-1-4-195.
838
839 Nasdala L., Irmer G., and Wolf D. 1995. The degree of metamictization in zircon: a Raman
840 spectroscopic study. *European Journal of Mineralogy* 7:471-478.
841
842 Nasdala L., Pidgeon R. T., Wolf D. 1996. Heterogeneous metamictization of zircon on a microscale,
843 *Geochimica et Cosmochimica Acta* 60:1091-1097.
844
845 Nasdala L., Götze J., Pidgeon R. T., Kempe U., and Seifert T. 1998. Constraining a SHRIMP U-Pb
846 age: microscale characterization of zircons from Saxionian Rotliegende rhyolites. *Contributions to*
847 *Mineralogy and Petrology* 132:300-306.
848
849 Nasdala L., Wenzel M., Varva G., Irmer G., Wenzel T., and Kober B. 2001. Metamictisation of
850 natural zircon: accumulation versus thermal annealing of radioactivity-induced damage.
851 *Contributions to Mineralogy and Petrology* 141:125-144.
852
853 Nasdala L., Reiners P.W., Garver J.I., Kennedy A.K., Stern R.A., Balan E., and Wirth R. (2004)
854 Incomplete retention of radiation damage in zircon from Sri Lanka. *American Mineralogist* 89:
855 219-231.
856
857 Palenik C. S., Nasdala L., and Ewing R. C. 2003. Radiation damage in zircon. *American Mineralogist*
858 88:777-781.
859
860 Powell M. A., Walker D., and Hays J. F. 1980. Experimental solidification of a eucrite basalt:
861 Microprobe studies (abstract). *Lunar and Planetary Science* 11:896-898.
862
863 Pun A. and Papike J. J. 1996. Unequilibrated eucrites and the equilibrated Juvinas eucrite: Pyroxene
864 REE systematics and major, minor, and trace element zoning. *American Mineralogist* 81:1438-
865 1451.
866
867 Righter K. and Drake M. J. 1997. A magma ocean on Vesta: core formation and petrogenesis of
868 eucrites and 471 diogenites. *Meteoritics & Planetary Science* 32:929-944.
869

870 Roeder P. L. and Reynolds I. 1991. Crystallization of chromite and chromium solubility in basaltic
871 melts. *Journal of Petrology* 32:909-934.
872

873 Roszjar J., Metzler K., Bischoff a., Greenwood R. C., and Franchi I. A. 2009a. Northwest Africa
874 (NWA) 5073 - An eucritic basalt with cm-sized pyroxenes (abstract). *Meteoritics & Planetary
875 Science* 44:5202.
876

877 Roszjar J., Geisler T., Scherer E. E., and Bischoff A. 2009b. The thermal history of zircon from the
878 NWA5073 eucrite as revealed by Raman spectroscopy (abstract). *Meteoritics & Planetary Science*
879 44:5203.
880

881 Roszjar J., Srinivasan G., Bischoff A., Mezger K., and Whitehouse M. 2009c. Hf-W ages of zircons -
882 New constraints on the evolution of the eucrite parent body (abstract #1655), 40th *Lunar and
883 Planetary Science Conference*.
884

885 Roszjar J. and Scherer E. E. 2010. Lu-Hf systematics of the NWA 5073 eucrite reflect a complex
886 thermal history (abstract). *Meteoritics & Planetary Science* 45:5425.
887

888 Rubin A. E. 1992. A shock-metamorphic model for silicate darkening and compositionally variable
889 plagioclase in CK and ordinary chondrites. *Geochimica et Cosmochimica Acta* 56:1705-1714.
890

891 Ruzicka A., Snyder G. A. and Taylor L. A. 1997. Vesta as the howardite, eucrite and diogenite parent
892 body: 477 implications for the size of a core and for large-scale differentiation. *Meteoritics &
893 Planetary Science* 32:825-840.
894

895 Saiki K., Takeda H., and Tabei T. 1990. Zircon in magnesian, basaltic eucrite Yamato 791438 and its
896 Possible Origin (abstract). *Lunar and Planetary Science* 21:341-349.
897

898 Scott E. R. D., Greenwood R. C., Franchi I. A. and Sanders I. S. 2009. Oxygen isotopic constraints on
899 the origin 489 and parent bodies of eucrites, diogenites, and howardites. *Geochimica et
900 Cosmochimica Acta* 73: 5835-5853.
901

902 Stelzner T., Heide K., Bischoff A., Weber A., Weber D., Scherer P., Schukz L., Happel M., Schrön
903 W., Neupert U., Michel R., Clayton R. N., Mayeda T. K., Bonani G., Haidas I., Ivy-Ochs S., and
904 Suter M. 1999. In interdisciplinary study of weathering effects in ordinary chondrites from the
905 Acfer region Algeria, *Meteoritics & Planetary Science* 34:787-794.
906

907 Stolper E. 1977. Experimental petrology of eucritic meteorites. *Geochimica et Cosmochimica Acta*
908 41:587-611.
909

910 Stöffler D., Bischoff A., Buchwald V., and Rubin A. E. 1988. Shock effects in meteorites. In
911 *Meteorites and the Early Solar System*, edited by Kerridge J. F. and Matthews J. F., Tucson:
912 University of Arizona Press, pp. 165-202.
913

914 Stöffler D., Keil K., and Scott E. R. D. 1991. Shock metamorphism of ordinary chondrites.
915 *Geochimica et Cosmochimica Acta* 55:3845-3867.
916

917 Takeda H. 1979. A layered-crust model of a howardite parent body. *Icarus* 40:455-470.
918

919 Takeda H. 1991. Comparison of Antarctic and non-Antarctic achondrites and possible origin of the
920 differences. *Geochimica et Cosmochimica Acta* 55:35-47.
921

922 Takeda H., and Yanai K. 1982. Mineralogical examination of the Yamato 79 achondrites: polymict
923 eucrites and ureilites. Proceedings 7th Symposium on Antarctic meteorites. pp. 97-123.
924

- 925 Takeda H. and Graham A. L. 1991. Degree of equilibrium of eucritic pyroxenes and thermal
926 metamorphism of the earliest planetary crust. *Meteoritics* 26:129-134.
927
- 928 Takeda H., Mori H., Yanai K., and Wooden J. L. 1982. Three different basalt types in Antarctic
929 polymict eucrites, a view from pyroxene chemical zoning trend (abstract), *Lunar and Planetary
930 Science* 13:792-293.
931
- 932 Takeda H., Mori H., Delaney J. S., Prinz M., Harlow G. E., and Ishii T. 1983. Mineralogical
933 comparison of antarctic and non-antarctic HED (howardites-eucrites-diogenites) achondrites.
934 Proceedings, 8th Symposium on Antarctic Meteorites. pp. 181-205.
935
- 936 Takeda H., Mori H., and Bogard D. D. 1994. Mineralogy and ³⁹Ar-⁴⁰Ar age of an old pristine basalt:
937 Thermal history of the HED parent body. *Earth and Planetary Science Letters* 122:183-194
938
- 939 Tanabe K. and Hiraishi J. 1980. Correction of finite slit width effects on Raman line widths.
940 *Spectrochimica Acta Part A: Molecular Spectroscopy* 36:341-344.
941
- 942 Walker D., Powell M. A., Lofgren G. E., and Hays J. F. 1978. Dynamic crystallization of a eucritic
943 basalt. Proceedings, 9th *Lunar and Planetary Science Conference*. pp. 1369-1391.
944
- 945 Warren P. H. 1997. Magnesium oxide-iron oxide mass balance constraints and a more detailed model
946 for the 502 relationship between eucrites and diogenites *Meteoritics & Planetary Science* 32:945-
947 963.
948
- 949 Warren P. H. 2002. Northwest Africa 1000: A new eucrite with maskelynite, unequilibrated pyroxene
950 crisscrossed by fayalite-rich veins, and Stannern-like geochemistry (abstract #1147). 33rd *Lunar
951 and Planetary Science Conference*.
952
- 953 Warren P. H. and Jerde E. 1987. Composition and origin of Nuevo Laredo trend eucrites. *Geochimica
954 et Cosmochimica Acta* 51:713-725.
955
- 956 Warren P. H. and Kallemeyn G. W. 2001. Eucrite Bluewing 001: a Stannern-like bulk composition
957 and its linkage with other unequilibrated HED basalts (abstract). *Lunar and Planetary Science*
958 32:2114.
959
- 960 Warren P. H., Jerde E. A., Migdisova L. F., Yaroshevsky A. A. 1990. Pomozdino: An anomalous,
961 high-MgO/FeO, yet REE-rich eucrite, Proceedings, 20th Lunar and Planetary Science Conference.
962 pp. 281-297.
963
- 964 Warren P. H., Kallemeyn G. W., Huber H., Ulff-Møller F., and Choe W. 2009. Siderophile and other
965 geochemical constraints on mixing relationships among HED-meteorite breccias. *Geochimica et
966 Cosmochimica Acta* 73:5918-5943.
967
- 968 Wiechert U. H., Halliday A. N., Palme H., and Rumble D. 2004. Oxygen isotope evidence for rapid
969 mixing of the HED parent body. *Earth and Planetary Science Letters* 221:373-382.
970
- 971 Wlotzka F. 1993. A weathering scale for the ordinary chondrites (abstract). *Meteoritics* 28:460.
972
- 973 Wopenka B., Jolliff B. L., Zinner E., and Kremser R. 1996. Trace element zoning and incipient
974 metamictization in a lunar zircon: Application of three microprobe techniques. *American
975 Mineralogist* 81:902-912.
976
- 977 Yamaguchi A. and Mikouchi T. 2005. Heating experiments of the HaH 262 eucrite and implication for
978 the metamorphic history of highly metamorphosed eucrites (abstract). *Lunar and Planetary Science*
979 36: 1574 (CD).
980

981 Yamaguchi A. and Misawa K. 2001. Occurrence and possible origin of zircon in basaltic eucrites
982 (abstract). *Antarctic Meteorites* 26:165-166.
983
984 Yamaguchi A., Taylor G. J., and Keil K. 1996. Global metamorphism on the eucrite parent body.
985 *Icarus* 124:97-112.
986
987 Yamaguchi A., Taylor G. J., Keil K., Floss C., Crozaz G., Nyquist L. E., Bogard D. D., Garrison D.
988 H., Wiesmann H., and Shih C.-Y. 2001. Post-crystallization reheating and partial melting of eucrite
989 EET90020 by impact into the hot crust of asteroid 4 Vesta ~4.50 Ga ago. *Geochimica et*
990 *Cosmochimica Acta* 65:3577-3599.
991
992 Yamaguchi A., Clayton R. N., Mayeda T. K., Ebihara M., Oura Y., Miura Y. N., Haramura H.,
993 Misawa K., Kojima H. and Nagao K. 2002. A new source of basaltic meteorites inferred from
994 Northwest Africa 011. *Science* 296:334-336.
995
996 Yamaguchi A., Barrat J. A., Greenwood R. C., Shirai N., Okamoto C., Setoyanagi T., Ebihara M.,
997 Franchi I. A., and Bohn M. 2009. Crustal partial melting on Vesta: Evidence from highly
998 metamorphosed eucrites. *Geochimica et Cosmochimica Acta* 73:7162-7182.
999
1000 Zhang M., Salje E. K. H., Farnan I., Graeme-Barber A., Daniel P., Ewing R. C., Clark A. M., Rios S.,
1001 and Leroux H. 2000a. Metamictization of zircon: Raman spectroscopic study. *Journal of Physics:*
1002 *Condensed Matter* 12:97-112.
1003
1004 Zhang M., Salje E. K. H., Farnan I., Capitani G. C., Leroux H., Clark A. M., Schlüter J., and Ewing R.
1005 C. 2000b. Annealing of α -decay damage in zircon: a Raman spectroscopic study. *Journal of*
1006 *Physics: Condensed Matter* 12:3131-3148.
1007
1008 Zhang M., Salje E. K. H., Ewing R. C., Farnan I., Rios S., Schlüter J., and Leggo P. 2000c. Alpha-
1009 decay damage and recrystallization in zircon: evidence for an intermediate state from infrared
1010 spectroscopy. *Journal of Physics: Condensed Matter* 12:5189-5199.
1011
1012
1013
1014
1015
1016

Table 1. Modal abundance of major phases
and mesostasis in NWA 5073 (vol.%).

Pyroxene phenocrysts	24.8
Primary feldspars (plagioclases)	26.4
Small pyroxenes	39.9
Mesostasis	8.5
Metal	0.4

Table 2. Chemical composition of mineral phases in NWA 5073. Results in wt.%.

	SiO ₂	TiO ₂	Al ₂ O ₃	Cr ₂ O ₃	FeO*	MnO	MgO	CaO	Na ₂ O	K ₂ O	P ₂ O ₅	HfO ₂	ZrO ₂	Y ₂ O ₃	Total	Endmembers average	Endmembers min. – max.	
Major phases																		
Pyroxene cores (n=27)	52.4	0.11	1.11	1.01	18.0	0.62	24.3	1.85	0.02	<0.01	n.d.	n.d.	n.d.	n.d.	99.41	En _{55.1} Wo _{4.2} Fs _{40.7}	En _{51.0-60.0} Wo _{1.7-7.6} Fs _{34.0-45.0}	
Pyroxene rims (n=27)	49.6	0.34	1.11	0.57	25.9	1.04	12.9	8.2	0.03	<0.01	n.d.	n.d.	n.d.	n.d.	99.68	En _{27.5} Wo _{17.4} Fs _{55.1}	En _{19.8-34.1} Wo _{8.2-33.8} Fs _{42.2-62.4}	
Small pyroxenes (n=11)	49.5	0.24	1.07	0.63	29.4	1.17	12.5	5.5	0.02	<0.01	n.d.	n.d.	n.d.	n.d.	100.01	En _{26.4} Wo _{11.6} Fs _{62.0}	En _{22.8-35.8} Wo _{5.9-18.8} Fs _{58.3-68.8}	
Pyroxenes mesostasis (n=5)	49.8	0.42	0.73	0.23	19.2	0.68	9.3	19.7	0.04	0.02	n.d.	n.d.	n.d.	n.d.	100.15	En _{27.1} Wo _{41.4} Fs _{31.5}	En _{25.7-27.9} Wo _{33.7-44.8} Fs _{27.7-40.7}	
Large Plagioclases (n=47)	47.4	0.02	32.3	<0.01	0.39	<0.01	0.10	16.9	1.65	0.16	n.d.	n.d.	n.d.	n.d.	99.00	An _{84.2} Ab _{14.9} Or _{0.9}	An _{77.0-88.9} Ab _{11.0-20.1} Or _{0.1-2.9}	
Plagioclases mesostasis (n=5)	51.0	0.03	30.1	0.02	0.65	<0.01	0.04	14.6	2.49	0.44	n.d.	n.d.	n.d.	n.d.	99.42	An _{74.4} Ab _{23.0} Or _{2.6}	An _{77.7-76.8} Ab _{20.4-24.9} Or _{2.0-3.5}	
Secondary Plagioclase (n=17)	43.0	n.d.	35.7	n.d.	1.38	n.d.	0.12	19.7	0.12	<0.01	n.d.	n.d.	n.d.	n.d.	100.00	An _{98.6} Ab _{1.3} Or _{0.1}	An _{97.2-100} Ab _{0-2.8} Or _{0-0.3}	
Minor phases																		
Chromite (n=5) [§]	<0.1	3.2	12.6	47.9	33.9	0.76	0.84	<0.1	n.d.	n.d.	n.d.	n.d.	n.d.	n.d.	99.78			
Ilmenite (n=13) [§]	<0.1	53.7	n.d.	<0.1	44.1	1.17	0.53	n.d.	n.d.	n.d.	n.d.	n.d.	n.d.	n.d.	99.81			
Apatite (n=19)	<0.01	n.d.	n.d.	n.d.	0.72	n.d.	<0.01	54.1	<0.01	n.d.	41.8	n.d.	n.d.	0.11	99.23			
Zircon (n=10)	32.4	n.d.	n.d.	n.d.	1.58	0.02	n.d.	0.06	n.d.	n.d.	0.14	1.31	66.2	0.16	101.83			
Tridymite (n=7)	98.9	0.07	0.23	0.03	0.36	<0.01	<0.01	0.13	<0.01	0.02	n.d.	n.d.	n.d.	n.d.	99.20			
Fe-rich olivine veins (n=16)	31.9	<0.01	0.06	0.19	53.1	1.46	14.4	0.05	<0.01	<0.01	n.d.	n.d.	n.d.	n.d.	101.13	Fo _{32.5} Fa _{67.5}	Fo ₂₉₋₃₅ Fa ₆₅₋₇₁	
Metal cores (n=13)	99.08	<0.01	0.16	<0.02	<0.02	<0.01	0.05	0.03	<0.01	<0.01	<0.01	<0.02	<0.02		99.33			

Data were obtained by EPMA; n.d. = not detected; *all Fe as FeO; zircon: Al was always below detection limit, high Fe content probably caused by contamination from surrounding phases such as ilmenite and Fe-metal; apatites: Cl and F average values are 0.3 and 4.0 wt.%, respectively; [§] Data obtained by SEM; chromite: V₂O₃ = 0.61 wt.%, ilmenite: V₂O₃ = 0.3 wt.%; for ilmenite and chromite: Ni was always below detection limit.

Table 3. Major and trace element composition of NWA 5073, compared to Stannern, Bouvante, and Nuevo Laredo. Oxides in wt.%, trace elements in $\mu\text{g/g}$. Eu/Eu^* and $\text{La}_n/\text{Yb}_n^*$ are calculated relative to CI average given by Evensen et al. (1978).

	NWA 5073	Stannern	Bouvante	Nuevo Laredo
Mass (g)	0.098	1.0	1.47	1.0 g
TiO ₂	0.77	1.08	1.06	0.94
Al ₂ O ₃	10.38	12.26	11.60	12.36
Cr ₂ O ₃	0.587	0.33	0.33	0.30
FeO	20.13	18.58	20.07	20.91
MnO	0.58	0.55	0.50	0.63
MgO	8.70	6.98	6.26	5.70
CaO	9.46	10.99	10.40	10.90
Na ₂ O	0.52	0.56	0.56	0.48
K ₂ O	0.09	0.09	0.10	0.06
P ₂ O ₅	0.097	0.10	0.14	0.09
Li	11.06	12.39	13.51	11.68
Be	0.32	0.44	0.42	0.37
Sc	25.8	30.2	30.8	35.8
V	78.51	56.90	55.20	60.10
Co	8.04	3.83	7.00	2.87
Ni	1.32	1.1	0.33	3.70
Cu	2.43	5.07	0.88	0.25
Zn	0.98	2.80	1.42	1.17
Ga	1.14	1.51	1.6	1.69
Rb	0.34	0.58	0.61	0.37
Sr	2131	92.7	93.7	84.4
Y	22.17	32.13	33.00	26.22
Zr	70.1	101	99.6	70.0
Nb	6.85	8.20	7.74	5.38
Cs	0.008	0.016	0.023	0.017
Ba	176	52.65	56.17	39.03
La	4.18	5.58	5.65	3.85
Ce	10.59	14.4	14.37	10.10
Pr	1.57	2.15	2.18	1.52
Nd	7.79	10.76	10.79	7.64
Sm	2.42	3.48	3.46	2.57
Eu	0.617	0.840	0.786	0.768
Gd	3.18	4.44	4.47	3.44
Tb	0.561	0.787	0.793	0.614
Dy	3.62	5.24	5.37	4.13
Ho	0.78	1.15	1.15	0.920
Er	2.22	3.26	3.26	2.67
Yb	2.04	3.06	2.87	2.56
Lu	0.291	0.434	0.421	0.366
Hf	1.77	2.51	2.52	1.83
Ta	0.365	0.441	0.413	0.292
W	0.193	0.174	0.165	0.105
Pb	0.24	(1.59)	0.32	0.26
Th	0.548	0.700	0.699	0.488
U	0.162	0.177	0.182	0.116
Eu/Eu*	0.68	0.65	0.61	0.79
La _n /Yb _n *	1.38	1.23	1.33	1.02

Table 4. LA-ICP-MS data of silicates in NWA 5073. Results in µg/g.

Pyroxene cores	1	2	3	4	5	6	7	8	single Px*	average (n=8)
La	0.010	0.025	0.005	0.005	0.013	0.007	0.021	0.008	0.366	0.012
Ce	0.032	0.058	0.027	0.016	0.047	0.024	0.050	0.028	1.302	0.035
Pr	0.009	0.013	0.004	0.004	0.010	0.004	0.010	0.008	0.276	0.008
Nd	0.066	0.081	0.027	0.029	0.068	0.032	0.063	0.064	1.726	0.054
Sm	0.068	0.054	0.020	0.037	0.059	0.020	0.048	0.050	0.883	0.044
Eu	0.011	0.008	0.004	0.007	0.008	0.005	0.009	0.008	0.054	0.007
Gd	0.127	0.143	0.038	0.062	0.098	0.055	0.095	0.117	1.486	0.092
Dy	0.244	0.240	0.067	0.131	0.169	0.096	0.171	0.228	2.297	0.168
Er	0.235	0.219	0.060	0.118	0.148	0.099	0.154	0.208	1.597	0.155
Yb	0.295	0.290	0.072	0.151	0.184	0.149	0.221	0.270	1.865	0.204
Lu	0.055	0.051	0.013	0.025	0.031	0.023	0.038	0.045	0.281	0.035
Plagioclase	1	2	3	4	5	6	7	average (n=7)		
La	0.243	0.350	0.522	0.308	0.328	0.286	0.194	0.319		
Ce	0.523	0.834	1.029	0.602	0.692	0.702	0.397	0.683		
Pr	0.064	0.101	0.124	0.076	0.087	0.088	0.053	0.085		
Nd	0.295	0.463	0.584	0.323	0.388	0.400	0.254	0.387		
Sm	0.099	0.133	0.164	0.095	0.089	0.126	0.081	0.112		
Eu	2.006	2.100	2.528	1.950	1.980	2.074	1.930	2.081		
Gd	0.067	0.124	0.154	0.082	0.083	0.101	0.064	0.096		
Dy	0.052	0.120	0.157	0.078	0.069	0.123	0.047	0.092		
Er	0.022	0.054	0.071	0.046	0.040	0.062	0.028	0.046		

* single small, Fe-rich pyroxene, found in close association to a mesostasis area; not used for average pyroxene calculation.

Table 5. U and Th concentrations, calculated α -decay dose, and frequencies and linewidths (FWHM) of the $\nu_3(\text{SiO}_4)$. Raman band of analyzed zircon grains from the NWA 5073 eucrite.

Zircon no.	U (ppm)	$\pm 2\sigma$	Th (ppm)	$\pm 2\sigma$	Dose (10^{16} α -events/mg)*	$\pm 2\sigma$ * ¹	Frequency (cm^{-1})* ²	FWHM (cm^{-1})* ²
Z1	<23	-	<20	-	<0.067		1000.5	9.9
Z3	<30	-	<20	-	<0.086		1001.2	8.5
Z4	<29	-	24	21	<0.093		1003.2	7.6
Z5	71	29	42	21	0.243	0.091	996.8	17.2
Z6	123	29	71	21	0.421	0.092	996.6	21.6
Z8	78	30	<21	-	0.255	0.096	999.3	12.1
Z9	105	29	86	21	0.372	0.092	998.2	18.8
Z10	75	30	<21	-	0.246	0.096	997.9	17.9
Z11	104	29	<21	-	0.334	0.092	997.2	25.8
Z13	160	29	120	21	0.559	0.092	991.7	25.3

*The dose was calculated for an inferred age of 4555 Ma; *¹Errors do not include the error of the inferred age;

1018
 1019
 1020
 1021
 1022
 1023
 1024
 1025
 1026
 1027
 1028
 1029
 1030
 1031
 1032
 1033

1034 **Figure Captions:**

1035

1036 **Fig. 1:** (a) Sawn surface of a section from the 185 g main mass of NWA 5073. (b) Thin section of
1037 NWA 5073; transmitted light, crossed polarizers.

1038

1039 **Fig. 2:** Ternary phase diagram for pyroxenes (Px) analyzed in NWA 5073. Large pyroxenes preserved
1040 their initial magmatic signature, as seen by Mg-enriched pigeonite cores. The chemical composition of
1041 small pyroxenes is in the range of the rims of large pyroxene phenocrysts or even more Fe-enriched.
1042 Pyroxenes found in the mesostasis are clearly distinct as they are significantly enriched in Ca. For
1043 comparison, composition of pristine and metasomatized pyroxenes from NWA 2061 (dark gray, solid-
1044 lined areas) and Y-75011 (light gray, dashed-lined areas) are shown, as these two eucrites also contain
1045 secondary Ca-rich plagioclase. The latter data are taken from Barrat et al. (2011).

1046

1047 **Fig. 3:** BSE images of the bulk texture of NWA 5073 (a) and textural details of its Fe-rich olivine
1048 veins (b-d). (a) Mosaic of BSE images from a NWA 5073. (b-d) Detailed images illustrating
1049 prominent Fe-rich olivine veins that crosscut large pyroxene laths, while adjacent silicate grains are
1050 devoid of them. (b) Typical zoned pyroxene lath with $En_{57}Wo_5$ in the crystals core and $En_{28}Wo_{17}$ at the
1051 rim is crosscut by Fe-rich olivine veins that end abruptly towards adjacent plagioclases (Plg) and
1052 smaller pyroxenes (Px). (c) Pyroxene-plagioclase border that shows a clear restriction of Fe-rich
1053 olivine veins to large pyroxene crystals. (d) Enlarged Mg-rich core region of a large pyroxene lath
1054 that is crosscut by Fe-rich olivine veins (Fe_{67}) and Fe-diffusion pathways along cleavage planes. Olivine
1055 veins are often occupied by small chromite, and troilite (FeS) grains, and Sr-sulfate inclusions, with
1056 the latter being a weathering product. Fe-rich areas that are aligned parallel to the olivine veinlets are
1057 probably formed by solid-state Fe-diffusion.

1058

1059 **Fig. 4:** BSE images of secondary phases in NWA 5073. (a) and (b): Fe-rich olivine veins (Ol) in large
1060 pyroxene (Px) and Fe-diffusion paths into their pyroxene host along cleavage planes: Cc = calcite
1061 (terrestrial weathering). (c) and (d): Secondary, Ca-rich plagioclase typically 5-20 μ m in diameter that
1062 were usually found in close association with Fe-rich olivine veins (Ol), are highlighted in ellipses.
1063 They are chemically distinct to adjacent large plagioclase (Plg).

1064

1065 **Fig. 5:** Ternary feldspar diagram illustrating three distinct plagioclase (Plg) types. Small plagioclase
1066 grains, located in the mesostasis, are slightly more Ab-rich (An_{72-77}) compared to larger plagioclase
1067 laths, which scatter to slightly higher An values (An_{72-89}). Secondary plagioclase is extremely enriched
1068 in Ca with An_{97-100} .

1069

1070 **Fig. 6:** BSE images (a) and (c) of representative zircon grains (Zr), selected for μ -Raman spectroscopy
1071 and EPMA analyses. Zircon grains typically occur in association with ilmenite (Ilm), plagioclase
1072 (Plg), Ca-pyroxene (Ca-Px), and silica (SiO_2). Corresponding cathodoluminescence images are given
1073 in (b) and (d). Zircon positions are highlighted as dashed areas.

1074

1075 **Fig. 7:** Diagram for bulk rock TiO_2 vs. FeO_{total}/MgO of basaltic, including residual, eucrite samples.
1076 The field of the basaltic eucrites has been drawn from a compilation of more than 170 analyses mainly
1077 from Warren et al. (2009), references listed in Barrat et al. (2007), and the residual eucrites from
1078 Yamaguchi et al. (2009). Residual eucrites cannot be distinguished from the basaltic eucrites in this
1079 diagram.

1080

1081 **Fig. 8:** Rare Earth Element (REE) abundances relative to CI chondritic abundance (Evensen et al.,
1082 1978), given for NWA 5073 bulk rock in comparison to Stannern, NWA4523, Juvinas, and Nuevo
1083 Laredo.

1084

1085 **Fig. 9:** Trace element pattern for NWA 5073 bulk rock compared to the Stannern-trend eucrites,
1086 including Stannern and NWA 4523, and Nuevo Laredo and Juvinas eucrites. All data are given
1087 relative to the Juvinas eucrite. Sr and Ba values of NWA 5073 whole rock are high (2131 and 176
1088 ppm, respectively), probably due to terrestrial weathering (Stelzner et al., 1999) and thus are excluded
1089 from this diagram.

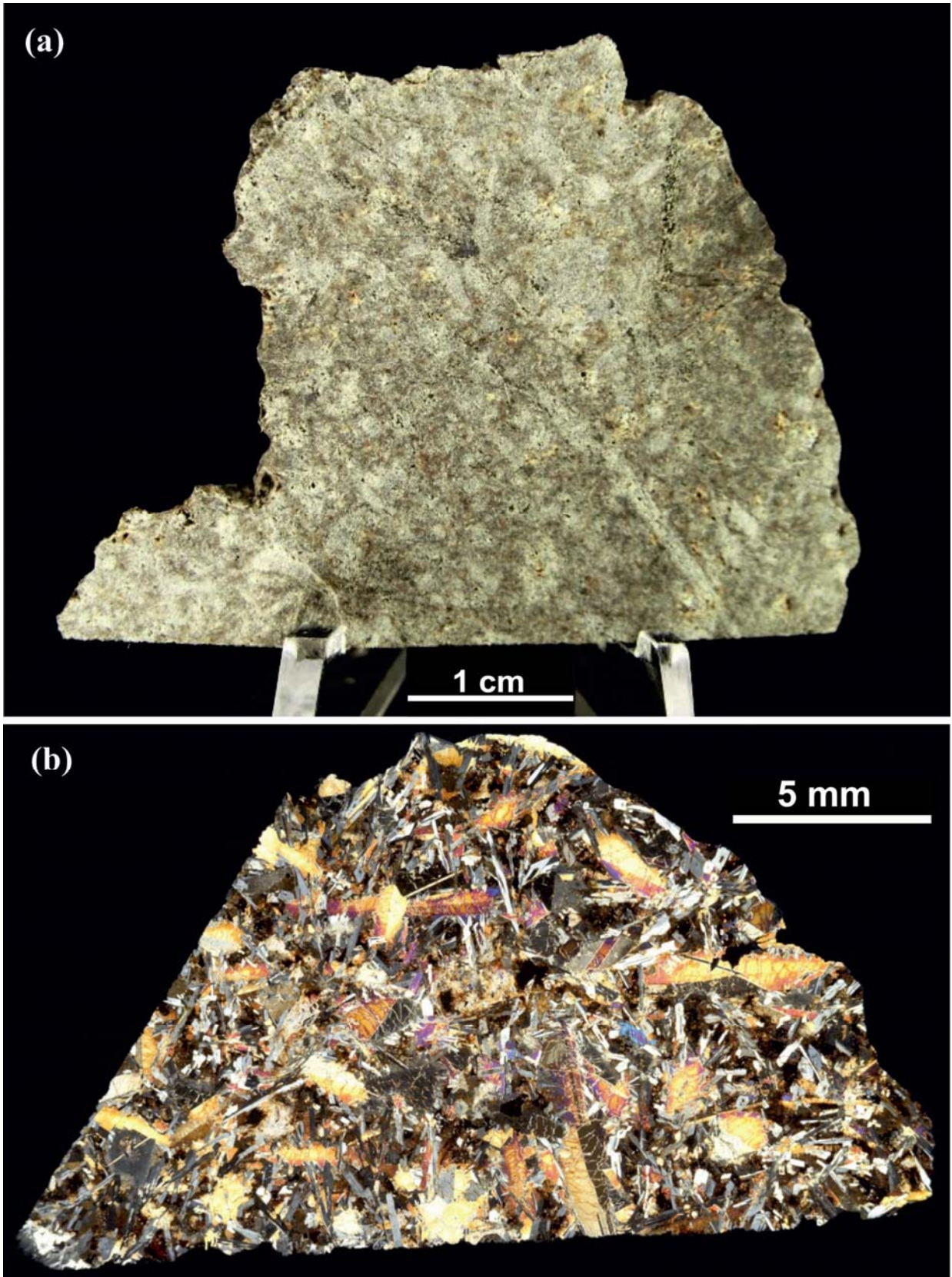
1090
1091
1092
1093
1094
1095
1096
1097
1098
1099
1100
1101
1102
1103
1104
1105
1106
1107
1108
1109
1110
1111
1112
1113
1114
1115
1116
1117
1118
1119
1120
1121
1122
1123
1124
1125
1126
1127
1128
1129
1130
1131
1132
1133
1134
1135
1136
1137
1138
1139

Fig. 10: REE pattern for plagioclase and pyroxene grains analyzed in NWA 5073. Average plagioclase (n=7) is shown by black squares, minimum and maximum values of all analyzed plagioclase grains are reported within the data range highlighted in light gray. The average of pigeonite cores (n=8) is given by white triangles. Data range for all analyzed pigeonite cores is highlighted in dark gray. One single small, Fe-rich pyroxene (light gray circles), closely associated with a mesostasis area, is extremely enriched in REE (Lu 10×CI). This analysis has not been used for average pyroxene core calculation.

Fig. 11: Oxygen isotope data for NWA 5073 compared to other eucrites (monomict, polymict, and cumulate eucrites), howardites, diogenites, and angrites. $\Delta^{17}\text{O}$ values are linearized (Miller, 2002). In this $\Delta^{17}\text{O}$ versus $\delta^{18}\text{O}$ diagram, samples formed from a homogeneous reservoir that subsequently fractionated by mass-dependent processes, plot along horizontal lines. Silicate minerals on Earth have isotopic compositions consistent with mass-dependent fractionation from a single reservoir, and define the terrestrial fractionation line (TFL). Angrites define a second horizontal line, the angrite fractionation line (AFL), with a mean $\Delta^{17}\text{O}$ value of -0.072 ± 0.007 (1σ). If polymict breccias are excluded, remaining HED samples also show limited $\Delta^{17}\text{O}$ variation and define a single eucrite fractionation line (EFL) with a mean $\Delta^{17}\text{O}$ value of -0.239 ± 0.007 (1σ). Diagram modified after Greenwood et al. (2005).

Fig. 12: Representative Raman spectra of five single zircon grains in sample NWA 5073 reveal a decreased frequency and an increased broadening of the $\nu_3(\text{SiO}_4)$ stretching band near $\sim 1008 \text{ cm}^{-1}$ (dashed line) with increasing radiation dose (D). The calculated α -dose, given within 2σ uncertainties, and expressed per $10^{16} \times \alpha$ -decay events/mg sample, is shown close to the spectra for each zircon crystal. Single zircon analyses are presented relative to a pure, synthetic, crystalline zircon (gray), taken from the RRUFF Raman data base.

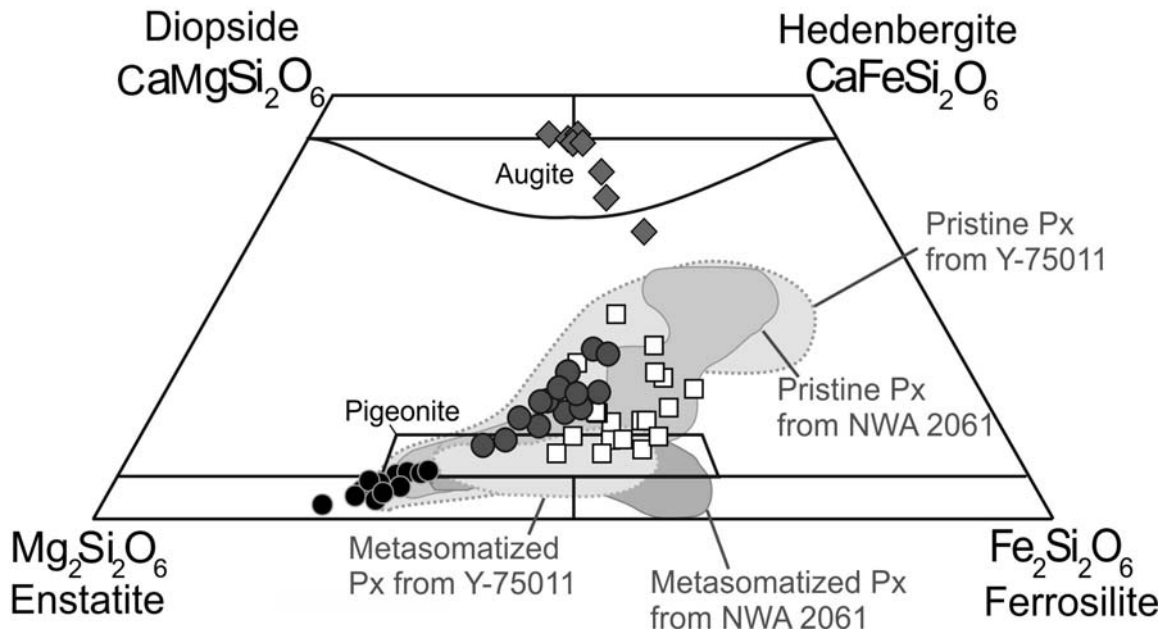
Fig. 13: (a) Diagram of the frequency of the $\nu_3(\text{SiO}_4)$ band analyzed in ten zircon crystals in NWA 5073 plotted against the measured linewidth of this band (given as full width at half maximum, FWHM). The radiation damage trend (RDT, gray field) is defined by variably, self-irradiation-damaged, terrestrial zircons (Saxonian rhyolites and Sri Lanka zircons data from Nasdala et al., 1998; 2004; Zhang et al., 2001a, b; own unpubl. data). A synthetic, non-metamict zircon is also plotted. Recent episodic annealing of heavily metamict zircon would shift the data points to the upper right in this diagram (highlighted by arrows), as indicated by dry heating experiments (Geisler et al., 2001; Geisler, 2002). **(b)** Plot of the linewidth (FWHM) of the $\nu_3(\text{SiO}_4)$ band vs. the α -decay dose (calculated accumulated radiation dose) for all analyzed zircon grains in NWA 5073. Uncertainties are in the range of 2σ . All data points plot below the radiation damage accumulation curve defined by Palenik et al. (2003), unambiguously indicating post-crystallization thermal annealing. Note that annealing of the NWA 5073 zircons is also obvious when compared with the Saxonian rhyolite zircons, which have neither episodically nor continuously been annealed (Nasdala et al., 1998) and were used to determine the damage accumulation curve. For more details of how the damage accumulation curve was defined see Palenik et al. (2003).



1140
1141
1142
1143
1144

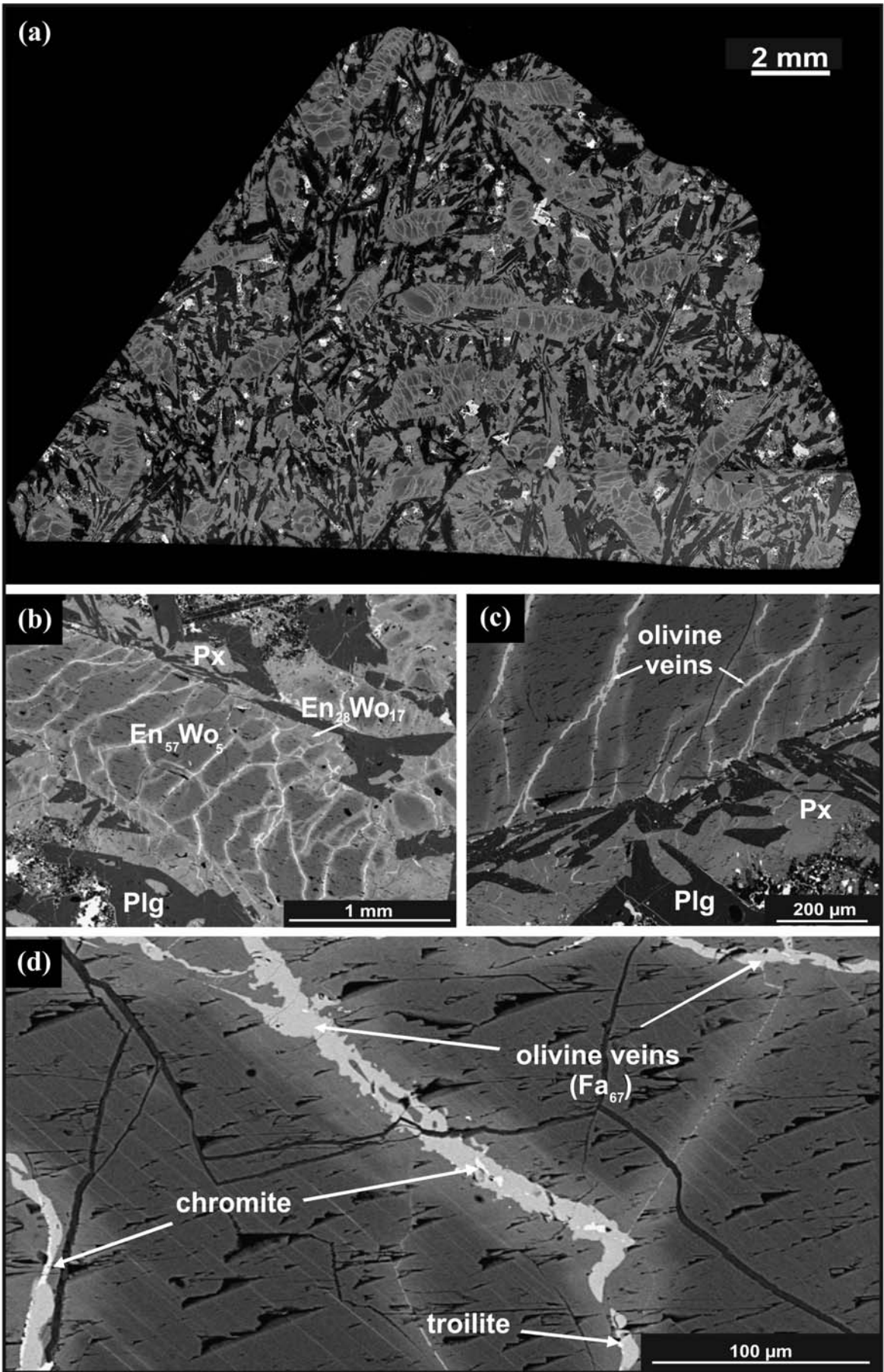
Fig.1

- Large Px (cores) ◆ Ca-Px (mesostasis)
- Large Px (rims) □ Small Px



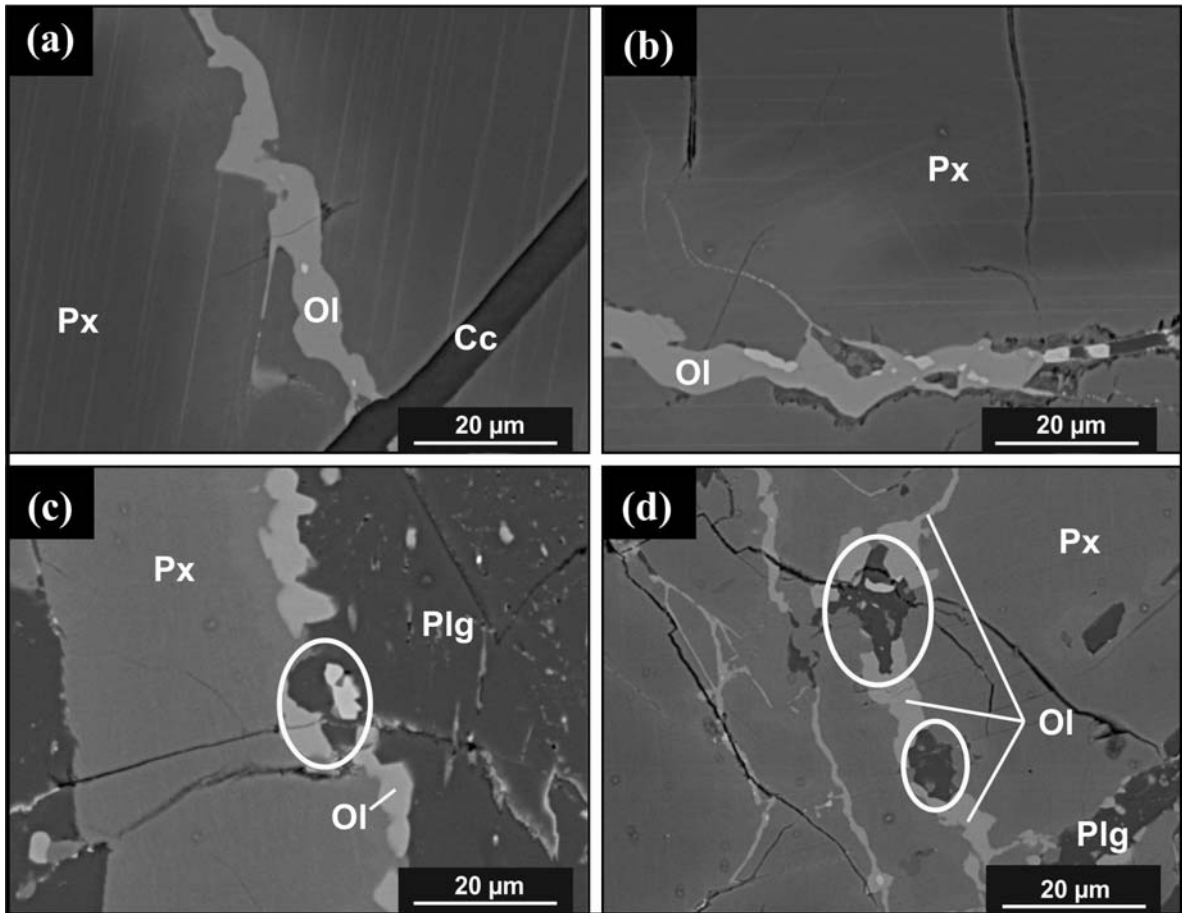
1145
1146
1147
1148
1149

Fig.2



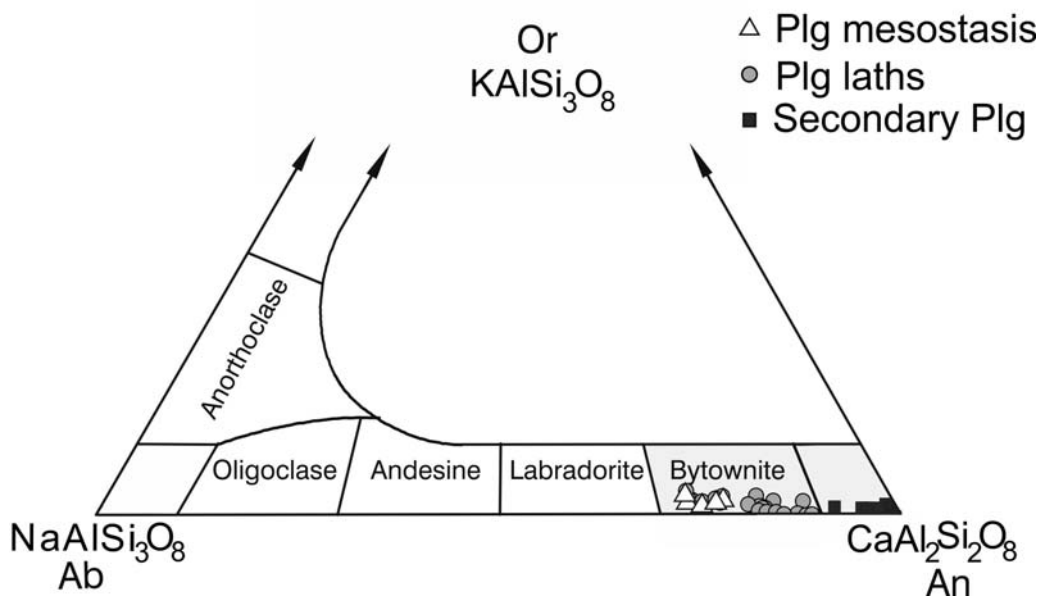
1150
1151
1152

Fig.3



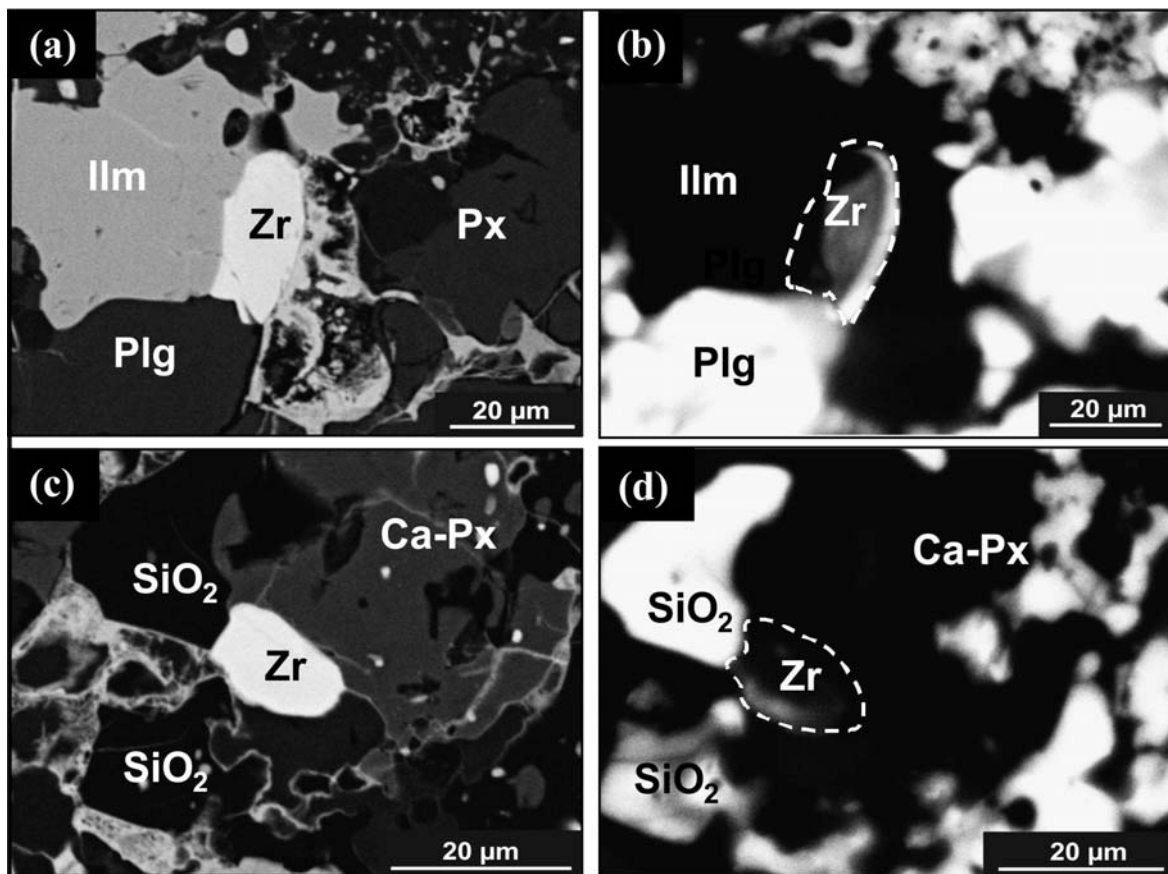
1153
1154
1155
1156

Fig.4



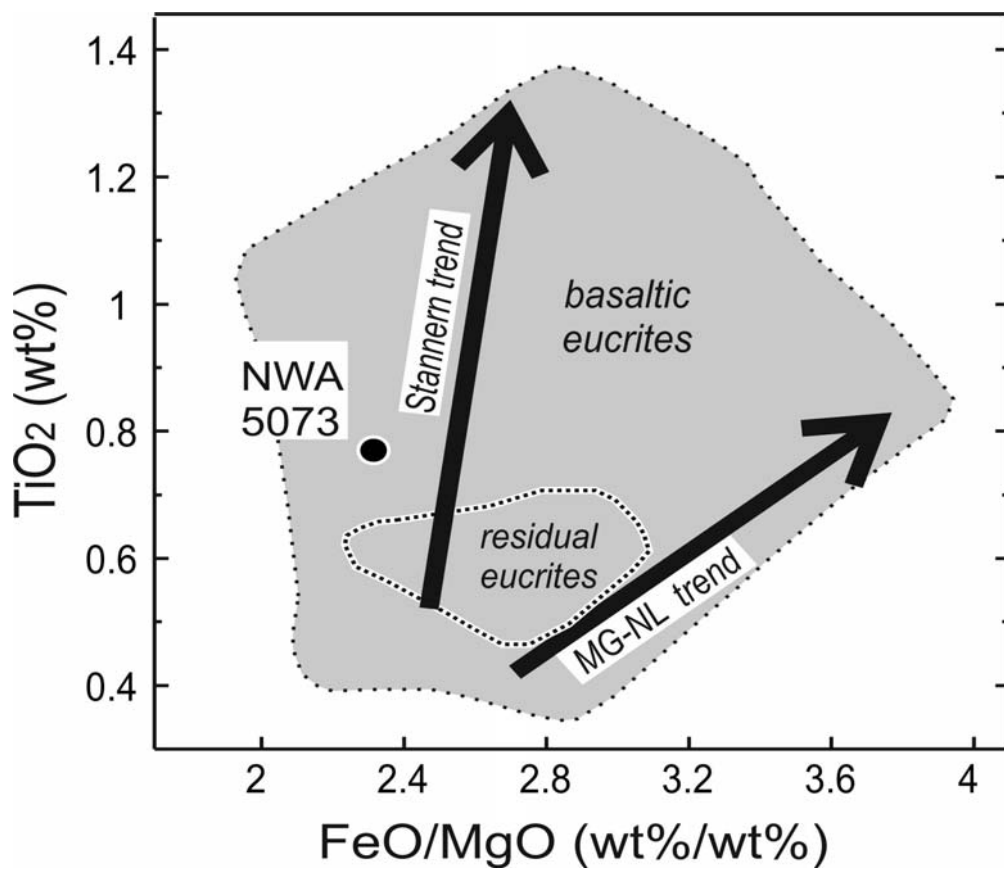
1157
1158
1159

Fig.5



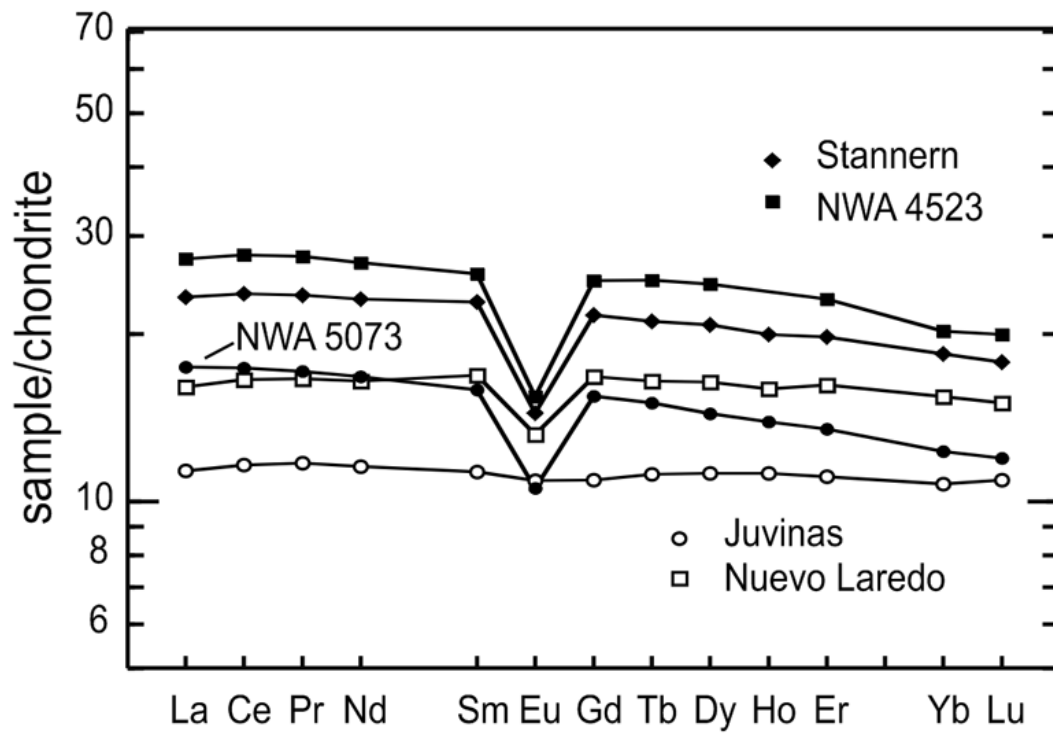
1160
1161
1162
1163

Fig.6

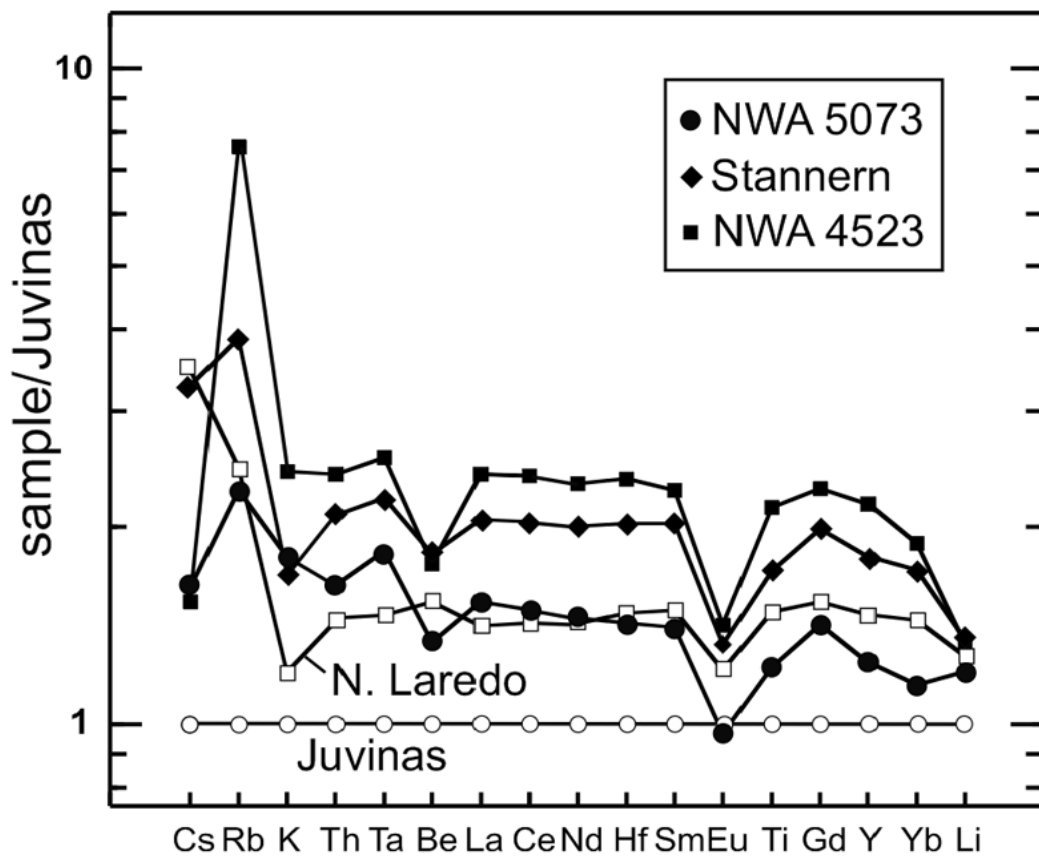


1164
1165
1166

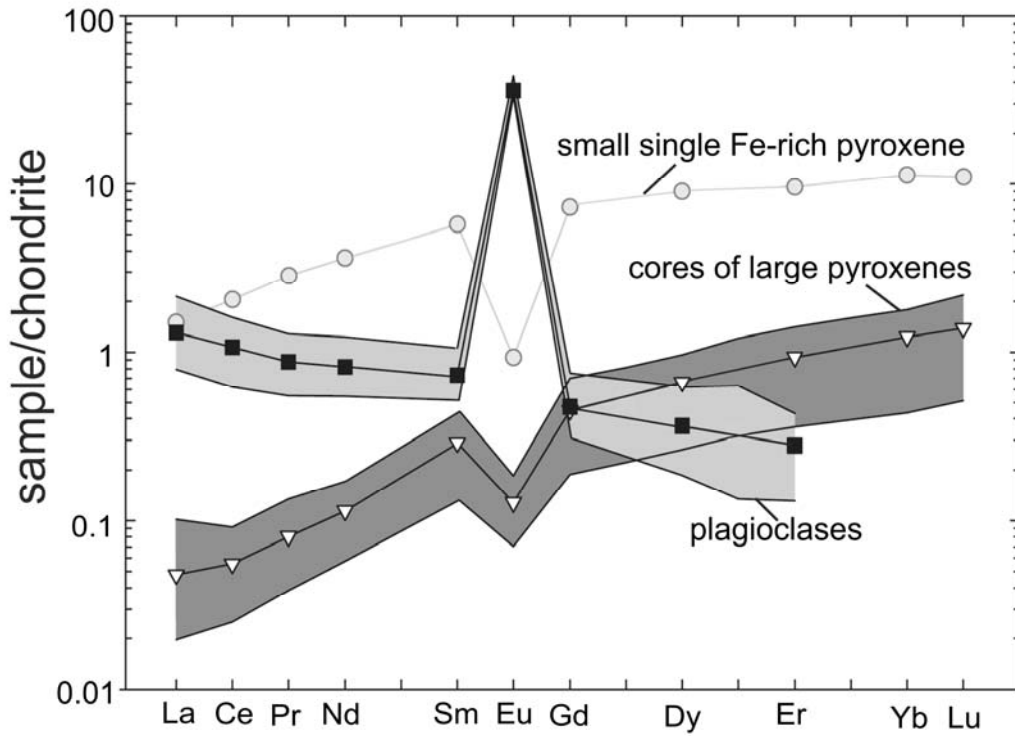
Fig.7



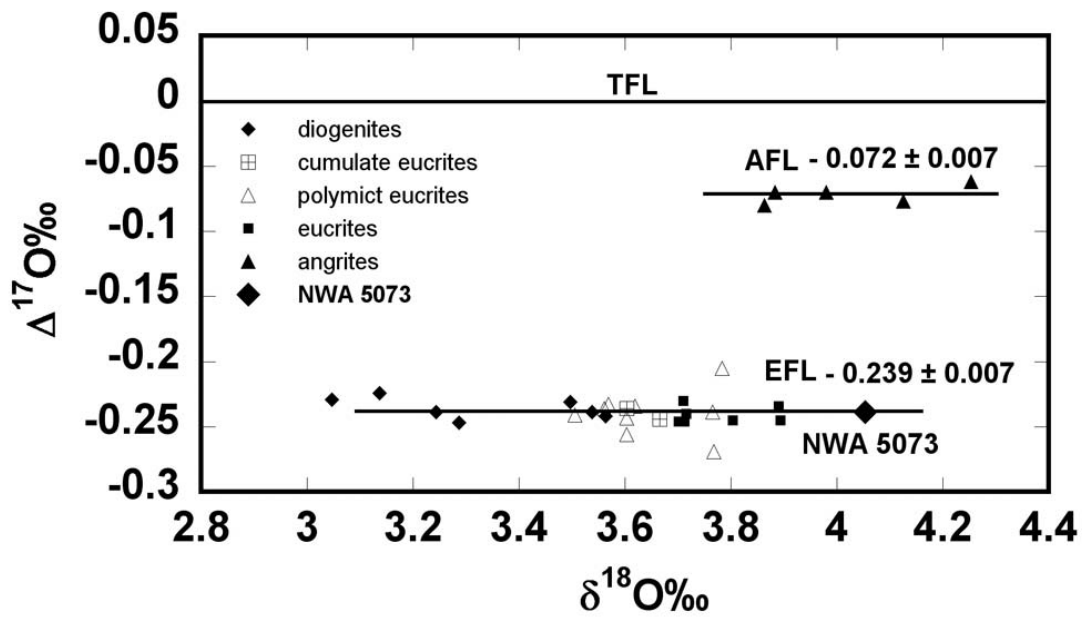
1167
1168 Fig.8
1169
1170



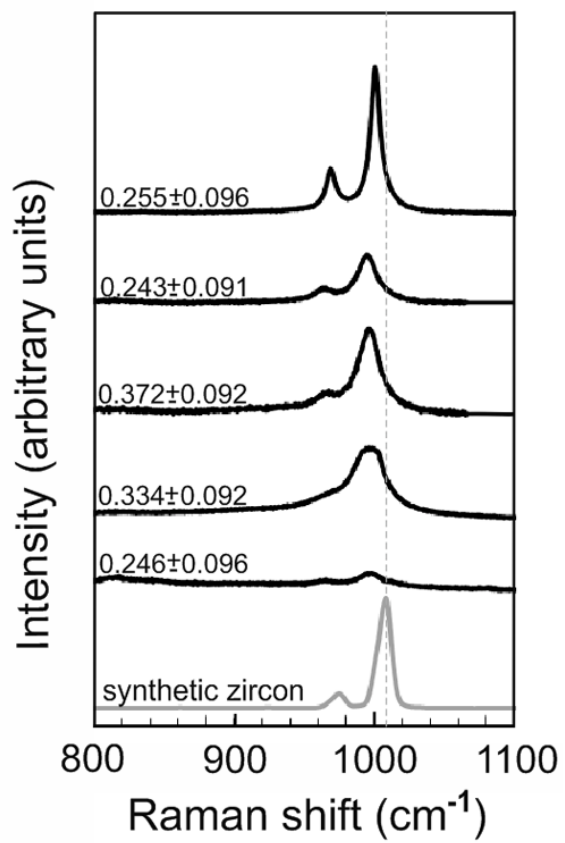
1171
1172 Fig.9
1173
1174



1175
1176 Fig.10
1177



1178
1179 Fi.11
1180
1181
1182
1183
1184



1185
1186
1187
1188
1189
1190

Fig.12

